Prospects for the Measurement of the Higgs CP Structure at ATLAS in Higgs to Four Lepton Decays

by

Michael Jarrett

B.Sc., University of Guelph, 2007

A Thesis Submitted in Partial Fulfillment of the

Requirements for the Degree of

MASTER OF SCIENCE

in the Department of Physics and Astronomy

Prospects for the Measurement of the Higgs CP Structure at ATLAS in Higgs to Four Lepton Decays

by

Michael Jarrett

B.Sc., University of Guelph, 2007

Supervisory Committee

Dr. J. Albert, Supervisor

(Department of Physics and Astronomy)

Dr. M. Lefebvre, Member

(Department of Physics and Astronomy)

Supervisory Committee

Dr. J. Albert, Supervisor

(Department of Physics and Astronomy)

Dr. M. Lefebvre, Member

(Department of Physics and Astronomy)

ABSTRACT

A Monte Carlo simulation is performed of Higgs decays in the $H \to ZZ \to 4l$ channel at ATLAS. Decay parameters are varied in order to model Higgs decays of differing CP states. A full analysis is performed, including trigger and background studies. Using various angular distributions as observables it is found that ATLAS should be able to exclude an anomalous CP odd coupling at 50 fb^{-1} and an anomalous CP even coupling at 100 fb^{-1}. The CP violating case studied could not be excluded.

Contents

List of Tables

List of Figures

Acknowledgements

Thanks to Eric Ouellete, Greg King and Dr. Justin Albert for their help and support in completing this thesis.

Special thanks to my parents for their love and encouragement.

Chapter 1

Introduction

The Standard Model has been the accepted theory of particle physics for several decades. Though its predictions have been confirmed by a large number of experiments, there have also been tantalizing hints of what is to come as higher energy scales are explored. The Large Hadron collider (LHC) was built to explore these new possibilities. Located outside Geneva, Switzerland, in a circular tunnel 27 km around and 100 m deep, two beams of protons will be collided at record energies of up to 7 TeV per beam. The resulting collisions will probe physics beyond the reach of any other experiment on earth.

A Toroidal LHC ApparatuS (ATLAS) is one of the two general purpose detectors at the LHC. One of the principle goals of ATLAS is to discover the Higgs boson, the only particle predicted by the Standard Model which is yet to be observed. There are compelling reasons to expect the Standard Model Higgs, or a Higgs-like particle will be observed in the energy range accessible to the LHC. It will be a crucial test of the capabilities of the ATLAS detector to determine the properties of the Higgs once a signal is observed, in order to determine whether the signal is consistent with the Standard Model, or whether some new physics is being observed.

This work will explore the capability of ATLAS to use the angular distributions of the four final state leptons in $H \to ZZ \to 4l$ decays to measure the CP properties of the Higgs. Chapter 2 will explore motivations for the existence of the Higgs, why CP is an important quantity, and how it can be accessed through angular distributions. Chapter 3 will discuss the capabilities and limitations of the ATLAS, particularly in measuring and recording leptonic final states. Since this work relies on simulated data, Chapter 4 will discuss the process of generating physics events using Monte Carlo simulations. Finally, Chapter 5 will examine the process of selecting signal over background events, and will attempt to demonstrate the ways in which the CP structure of the Higgs can be explored using the available data. Unless otherwise noted, this work uses natural units ($c = \hbar = 1$).

Chapter 2

Theoretical Background

The Standard Model is the currently accepted theory of fundamental particle physics. It has successfully predicted the observations of every particle discovered since its development thirty years ago. The Higgs boson, necessary for the self-consistency of the theory, is the only remaining particle which has been predicted but which has yet to be discovered. In the coming years, the ATLAS detector at the LHC is expected to observe a signal consistent with a Standard Model Higgs boson. One of the channels in which this discovery is likely to occur is the decay of the Higgs to two Z bosons (at least one of which may be off its mass shell), which decay further to lepton anti-lepton pairs which are the final state observed in the detector (in this analysis, leptons are considered electrons and muons). This chapter will discuss the necessity that once a Higgs signal is observed, a detailed analysis is undertaken to measure the properties of the new particle in order to test Standard Model predictions.

2.1 Higgs Boson in the Standard Model

The Higgs field was postulated during the development of electroweak theory in order to solve a specific problem: that Goldstone's theorem [4] seemed to demand that the

bosons which carry the weak force must be massless, but experiments had already put lower bounds on the masses of these particles [5]. The Higgs mechanism, which postulates a new scalar field in the form of a complex scalar doublet,

$$\phi = \begin{pmatrix} \phi^+ \\ \phi^0 \end{pmatrix}, \tag{2.1}$$

with four degrees of freedom, circumvents Goldstone's theorem. Three of the degrees of freedom of the Higgs field "swallow up" [6] the Goldstone bosons, giving them mass and turning them into the $W^{\pm}$ and Z bosons. The remaining Goldstone boson is the massless photon, and the remaining component of the Higgs field becomes the physical Higgs boson.

There are other motivations for having a scalar field in the unified Electroweak theory. The Higgs field also provides a mechanism for giving mass to the fermions. The Higgs field permeates the vacuum, and its coupling is proportional to particle masses. Therefore a particle moving through the vacuum obtains its inertial mass through interactions with the Higgs field.

A third motivation for the Higgs field is the necessity of unitarity in Electroweak perturbative field theory. Relevant quantities in particle physics such as cross sections and decay amplitudes are calculated by expanding about a constant and then calculating to the desired order. For this method to be valid, we expect lower order terms to give approximate physical values, with higher order terms adding smaller corrections. If one attempts to calculate the scattering amplitude in $W^+W^- \rightarrow W^+W^-$ scattering to first order using only γ and Z as propagators, it is found that the amplitude scales with the centre of mass energy, $\sqrt{s}$. This is a non-physical result, since it implies that the probability of two vector bosons scattering cannot be normalized to 1. If, however, the first order diagrams which include a scalar particle as a propagator are included, the amplitude peaks then goes to zero at high $\sqrt{s}$, restoring unitarity.

This analysis also puts a theoretical mass limit on the Higgs, since a no-Higgs model is equivalent to a $M_H = \infty$ model. Therefore there must be some cut-off less than infinity at which a Higgs particle restores unitarity. Using an analysis such as this, that limit has been found to be approximately 850 GeV [7] . This is not a hard limit for a Higgs mass; it only implies that perturbation theory will no longer apply above this mass range, since the Higgs self-interaction would be too strong. However, it strongly suggests that since perturbation theory appears to hold for all other electroweak phenomena that have been investigated, there must be some new boson in the mass range below 1 TeV.

2.2 Higgs Physics Beyond the Standard Model

The previous section described various reasons for which a new particle is expected to be found in the mass range accessible at the LHC. These ideas, however, aren't limited to the Standard Model. The Standard Model uses the "Minimal Higgs Model", which is the simplest model that can provide spontaneous symmetry breaking. A more complex Higgs sector could satisfy the requirements for a Higgs field discussed previously while also giving rise to exotic phenomena.

Supersymmetry is one of the most promising extensions of the Standard Model. It postulates "super partners" of all known SM particles which have the same quantities as their SM partner, except for their spin which differs by $\frac{1}{2}$. In the simplest implementation of supersymmetry, known as the Minimal Supersymmetric Standard Model (MSSM), the Higgs field is made up of two complex scalar doublets, instead of the one doublet in the Standard Model. Following the same logic as before, this leaves 5 degrees of freedom not taken up by the massive vector bosons, implying 5 massive scalar particles. Table 2.1 lists the MSSM Higgs particles and their expected

properties.

Particle	Charge	J^{PC}	J^P
H^0	0	0^{++}	
h^0	0	0^{++}	
A^0	0	0^{+-}	
H^+	+1		0^+
H^-	–1		0^+

Table 2.1: The 5 Higgs particles in the MSSM Higgs sector

It is apparent, therefore, that observing a Higgs signal which is not consistent with a single, neutral, scalar, CP even particle would be definite evidence for physics beyond the Standard Model. Determining how sensitive the ATLAS detector will be to such measurements is the central purpose of this work.

2.3 Charge Conjugation and Parity Symmetries

Parity ($\hat{P}$) and Charge Conjugation ($\hat{C}$) are two of the three principle discrete symmetries in nature. Parity is the mirror, or inversion, symmetry. It is the principle that a physical process inverted through all 3 dimensions should also be a physical process. All particles are in parity eigenstates of either 1 or -1, and parity is multiplicatively conserved in all strong and electromagnetic interactions. Charge conjugation flips all internal quantum numbers (charge, baryon number, lepton number, etc.) to their negative but leaves mass, energy and spin unchanged. Effectively, it turns a particle into its anti-particle. Neutral particles are in $\hat{C}$ eigenstates, and it is conserved by the same type of interactions as parity. They are both maximally violated individually in weak interactions, but the composite symmetry, CP, is only rarely violated.

Breaking CP symmetry effectively provides a mechanism by which particles can be distinguished empirically from anti-particles. This distinction had previously been arbitrary, based only on which types of matter are stable in nature. CP violation

(CPV) is predicted in small amounts by the Standard Model, and has been directly observed in $K^0\bar{K^0}$ [8] and $B^0\bar{B^0}$ [9] systems. CPV carries an important cosmological implication since it provides a mechanism by which the universe can be filled with matter instead of anti-matter or nothing. Big Bang Theory predicts that equal amounts of matter and anti-matter were created at the beginning of the Universe, and if CP were a perfect symmetry, all the particles would have annihilated each other instead of forming stable particles. However, Standard Model CPV is not considered to be enough to explain the matter–anti-matter asymmetry of the Universe, and so other sources of CPV are still being sought. Observing CPV in the Higgs sector could contribute the solution of this puzzle.

2.4 The Model Independent Coupling

A Higgs particle created at ATLAS is expected to decay according to the branching fractions in Figure 2.1, depending on its mass. With a fully resolvable final state, the $H \to ZZ \to 4$ lepton decay is expected to be the cleanest channel in which to observe a Higgs decay [2, 10, 11]. To obtain CP information from this decay, a model independent parametrization of the HZZ coupling was used [2]:

$$V_{\mu\nu}^{HZZ} = \frac{igm_Z}{\cos\theta_W}\left[Ag_{\mu\nu} + B\frac{p_\mu p_\nu}{m_Z^2} + C\epsilon_{\mu\nu\alpha\beta}\frac{p^\alpha k^\beta}{m_Z^2}\right]. \tag{2.2}$$

In this equation $p = q_1 + q_2$ and $k = q_1 - q_2$, q_i are the four-momenta of the Z bosons, θ_W is the weak mixing angle, and $\epsilon_{\mu\nu\alpha\beta}$ is the antisymmetric tensor. This coupling allows one to create an HZZ coupling for a Higgs with either CP quantum number, or for a CP violating Higgs, simply by varying the constants A, B and C. The coupling with $B = C = 0$ and a non-zero A corresponds to the Standard Model Higgs; $A = C = 0$ with a non-zero B is a non-SM CP-even Higgs; and $A = B = 0$

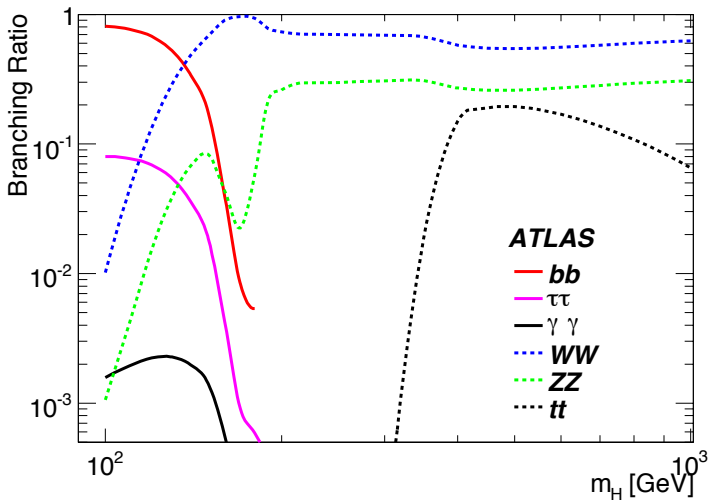

Figure 2.1: Expected branching ratios in Higgs decays [1].

with non-zero C is a non-SM CP-odd Higgs, consistent with the pseudoscalar Higgs in MSSM. In principle, any combination of values for A, B and C are allowed, and though A must be a real number, B and C may be complex. The CP violating case occurs when C along with either A or B are non-zero. In this work, $(1, 0, 0)$, $(0, 1, 0)$, $(0, 0, 1)$ and $(1, 0, 1)$ are chosen as representative cases of the different possible combinations. The reasons for the choice of these test cases will be addressed shortly.

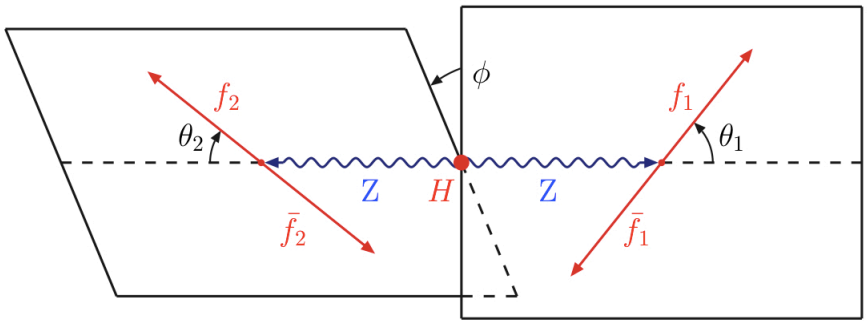

Figure 2.2: Visualization of a Higgs decay in terms of the angles ϕ and θ [2].

There are two relevant observable quantities which must now be defined: the angles ϕ and θ. These angles characterize the decay of the Higgs boson into the two Z bosons, and the Z bosons into four fermions. Figure 2.2 shows the angles on a schematic of a Higgs decay. The decaying Z bosons each form a plane defined by the momenta of the daughter leptons. The angle between these two planes in the Higgs rest frame is labelled ϕ. In each Z rest frame, θ is the angle between the line of flight of the Z and the momentum of its daughter lepton (not anti-lepton). They are labelled θ_1 and θ_2.

The differential decay rate can be written in terms of ϕ and $\cos\theta$ as [2]:

$$
\begin{aligned}
\frac{d^3\Gamma}{d\cos\theta_1 d\cos\theta_2 d\phi} \sim \quad & A^2\left[\sin^2\theta_1\sin^2\theta_2 - \frac{1}{2\gamma_a}\sin 2\theta_1\sin 2\theta_2\cos\phi\right. \\
& + \frac{1}{2\gamma_a^2}[(1+\cos^2\theta_1)(1+\cos^2\theta_2) + \sin^2\theta_1\sin^2\theta_2\cos 2\phi] \\
& \left. - \frac{2\eta_1\eta_2}{\gamma_a}\left(\sin^2\theta_1\sin^2\theta_2\cos\phi - \frac{1}{\gamma_a}\cos\theta_1\cos\theta_2\right)\right] \\
& + |B|^2\frac{\gamma_b^4}{\gamma_a^2}x^2\sin^2\theta_1\sin^2\theta_2 \\
& + |C|^2\frac{\gamma_b^2}{\gamma_a^2}4x^2\left[1+\cos^2\theta_1\cos^2\theta_2 - \frac{1}{2}\sin^2\theta_1\sin^2\theta_2(1+\cos 2\phi)\right. \\
& \left. + 2\eta_1\eta_2\cos\theta_1\cos\theta_2\right] \\
& - 2A\Im m(B)\frac{\gamma_b^2}{\gamma_a^2}x\sin\theta_1\sin\theta_2\sin\phi[\eta_2\cos\theta_1 + \eta_1\cos\theta_2] \\
& - 2A\Re e(B)\frac{\gamma_b^2}{\gamma_a^2}x\left[-\gamma_a\sin^2\theta_1\sin^2\theta_2 + \frac{1}{4}\sin 2\theta_1\sin 2\theta_2\cos\phi\right. \\
& \left. + \eta_1\eta_2\sin\theta_1\sin\theta_2\cos\phi\right] \\
& - 2A\Im m(C)\frac{\gamma_b}{\gamma_a}2x\left[-\sin\theta_1\sin\theta_2\cos\phi(\eta_1\cos\theta_2 + \eta_2\cos\theta_1\right. \\
& \left. + \frac{1}{\gamma_a}\left(\eta_1\cos\theta_1(1+\cos^2\theta_2) + \eta_2\cos\theta_2(1+\cos^2\theta_1)\right)\right]
\end{aligned}
$$

$$
\begin{aligned}
&- 2A\Re e(C)\frac{\gamma_b}{\gamma_a}2x\sin\theta_1\sin\theta_2\sin\phi\left[-\cos\theta_1\cos\theta_2+\frac{\sin\theta_1\sin\theta_2}{\gamma_a}-\eta_1\eta_2\right]\\
&+ 2\Im m(B^*C)\frac{\gamma_b^3}{\gamma_a^2}2x^2\sin\theta_1\sin\theta_2\cos\phi\left[\eta_2\cos\theta_1+\eta_1\cos\theta_2\right]\\
&+ 2\Re e(B^*C)\frac{\gamma_b^3}{\gamma_a^2}2x^2\sin\theta_1\sin\theta_2\sin\phi\left[\cos\theta_1\cos\theta_2+\eta_1\eta_2\right]
\end{aligned}
\tag{2.3}
$$

where: $x = m_1 m_2/m_Z^2$, with m_i as the masses of the two Z bosons; $\gamma_a = \gamma_1\gamma_2(1+\beta_1\beta_2)$ and $\gamma_b = \gamma_1\gamma_2(\beta_1+\beta_2)$; γ_i are the Lorentz boost factors of the Z bosons, $\gamma_i = 1/\sqrt{1-\beta_i^2}$; The velocities of the two Z bosons in the Higgs rest frame are $\beta_i = m_H\beta/2E_i$, with

$$
\beta = \left\{\left[1-\frac{(m_1+m_2)^2}{m_H^2}\right]\left[1-\frac{(m_1-m_2)^2}{m_H^2}\right]\right\}^{1/2}. \tag{2.4}
$$

Finally, the η_i are combinations of the weak vector and axial vector coupling, ν_{f_i} and a_{f_i} such that

$$
\eta_i = \frac{2\nu_{f_i}a_{f_i}}{\nu_{f_i}^2+a_{f_i}^2} \tag{2.5}
$$

where $\nu_{f_i} = T_{f_i}^3 - 2Q_{f_i}\sin\theta_W{}^2$ and $a_{f_i} = T_{f_i}^3$. $T_{f_i}^3$ is the third component of the weak isospin and Q_{f_i} is the electric charge of each final state fermion, f_i.

In order to determine the nature of the $H \to ZZ$ coupling through experimental data, it is possible to construct observable quantities which can discriminate between the four cases for A,B and C described above. To do this, it is possible to integrate the above equation alternately over ϕ and $\cos\theta_i$ to obtain equations for the angular distributions in each observable. For simplicity, this can be done for each case separately, with constants collected.

For the angular distribution in ϕ, integrating over $\cos\theta_1$ and $\cos\theta_2$ in the Standard Model case ($A = 1, B = C = 0$) the decay rate becomes

$$\begin{aligned}\frac{d\Gamma}{d\phi} \sim & 1 + a_1 \cos\phi + a_2 \cos 2\phi, \\ a_1 = & -\frac{9\pi^2}{32}\eta_1\eta_2\frac{\gamma_a}{2+\gamma_a^2}, \\ a_2 = & \frac{1}{2(2+\gamma_a^2)}.\end{aligned} \tag{2.6}$$

For the pure pseudoscalar case ($A = B = 0, C = 1$), this becomes

$$\frac{d\Gamma}{d\phi} \sim 1 - \frac{16}{9}\frac{\gamma_b^2}{\gamma_a^2}x^2 \cos 2\phi, \tag{2.7}$$

and in the pure scalar case ($A = C = 0, B = 1$) it is

$$\frac{d\Gamma}{d\phi} \sim \frac{\gamma_b^4}{\gamma_a^2}x^2\frac{16}{9}$$

which has no ϕ dependance at all. Finally, the CP-violating coupling, with both A and C not equal to zero, becomes

$$\begin{aligned}\frac{d\Gamma}{d\phi} &\sim b_1 + b_2\cos\phi + b_3\cos 2\phi + b_4\sin\phi + b_5\sin 2\phi \\ b_1 &= A^2(2+\gamma_a^2) + 8|C|^2x^2\gamma_b^2 \\ b_2 &= -\frac{9\pi^2}{32}A^2\eta_1\eta_2\gamma_a \\ b_3 &= \frac{9\pi^2}{16}A\Re e(C)\eta_1\eta_2 x\gamma_a\gamma_b \\ b_4 &= \frac{A^2}{2} - 2|C|^2x^2\gamma_b^2 \\ b_5 &= -2A\Re e(C)x\gamma_b.\end{aligned} \tag{2.8}$$

It is apparent that all four cases can be considered special cases of the general

equation

$$\frac{d\Gamma}{d\phi} = \alpha\cos\phi + \beta\cos 2\phi + \gamma\sin\phi + \delta\sin 2\phi + K, \tag{2.9}$$

where the values of the coefficients α, β, γ and δ discriminate between the different CP states. The offset K is required to account for constant terms when fitting data to the equation, but has no relevance to the coupling.

The same process can be performed for $\cos\theta_1$. Integrating over ϕ and $\cos\theta_2$, in the Standard Model case

$$\frac{d\Gamma}{d\cos\theta_1} \sim \sin^2\theta_1 + \frac{2}{\gamma_a^2 - 1}, \tag{2.10}$$

for the CP odd case

$$\frac{d\Gamma}{d\cos\theta_1} \sim 1 + \cos^2\theta_1, \tag{2.11}$$

for the CP even case

$$\frac{d\Gamma}{d\cos\theta_1} \sim \frac{4}{3}\frac{\gamma_b^4}{\gamma_a^2}x^2(\sin^2\theta_1), \tag{2.12}$$

and finally for the CP-violating coupling,

$$\frac{d\Gamma}{d\cos\theta_1} \sim A^2\left[(\gamma_a^2 - 1)\sin^2\theta_1 + 2\right] + 4x^2\gamma_b^2(1 + \cos^2\theta_1). \tag{2.13}$$

The general form for the decay amplitude in $\cos\theta$ can be written as

$$\frac{d\Gamma}{d\cos\theta} = T(1 + \cos^2\theta) + L\sin^2\theta. \tag{2.14}$$

This form is chosen in order to take advantage of the fact that T and L correspond to the transverse and longitudinal polarizations, respectively, of the Z bosons, and

are not independent parameters. The parameter R, where

$$R = \frac{L - T}{L + T}, \tag{2.15}$$

corresponds to the ratio of the two polarizations for a given sample. The parameters α, β, γ and δ and R are therefore the parameters of interest for discriminating between the different possible CP states of the Higgs sector.

The reasoning behind the choices of the ABC coefficients in the four test cases defined above should now be clear. In the three pure cases, the magnitude of the coefficient does not affect the properties of the coupling. A must be real, so $A = 1$ is the simplest case. B and C may be complex, but in the pure cases the differential cross section only depends on their magnitude, so as long as values are chosen such that $|A| = |B| = 1$ the results will not be affected. Cross terms in B are not relevant to any new physics, and since distinction between the real and imaginary parts of B is only relevant in the cross terms, the complex nature of B can safely be ignored. Cross terms in A and C, however, must be considered due to the prospect of CP violation. Due to constraints on Monte Carlo simulation, only one CP violating case is considered. The $C = 1$ case was chosen as a test case since when C is purely imaginary, the coefficients γ and δ in the ϕ distribution go to zero, so a real value of C provides a more general case.

Chapter 3

The ATLAS Detector

3.1 The Large Hadron Collider

The Large Hadron Collider (LHC), located on the border between France and Switzerland is the largest particle accelerator in the world and began colliding protons in late 2009. It consists of two beam pipes, each approximately 27 km long, which accelerate protons to nearly the speed of light before colliding them at interaction points distributed around the ring. During the 2010-11 LHC run, the beams operate at 3.5 TeV, after which there will be a maintenance shutdown allowing the beam energy to be raised to the design value of 7 TeV.

The energy range accessible at the LHC is beyond anything previously achieved by particle accelerators, but rare events such as a Higgs decay will still occur at very low rates. For this reason, the LHC must provide a very large number of events. This is achieved with an extremely high design luminosity of 10^{34} cm^{-2}s^{-1}. The luminosity, $\mathscr{L}$, determines the rate at which a process with cross-section σ occurs through the relationship $r = \mathscr{L}\sigma$. The integrated luminosity is the cumulative luminosity over some time interval, and determines the number of events of a particular process

through the relationship $N = \sigma \int \mathscr{L} dt$. Cross-sections and luminosities are often measured in barns and inverse barns, respectively, where 1b= 10^{-28} m^2. At present, the LHC has provided to ATLAS an integrated luminosity of approximately 45 pb^{-1}. Tens to hundreds of fb^{-1} are expected to be provided over its lifetime.

Collisions at the LHC are between two beams of protons. Protons are made up of 3 valence quarks, the gluons which bind them together, and a multitude of virtual "sea" quarks, any of which can be involved in a given collision. The beam energy is the cumulative energy of the entire proton, and the energy of the constituent particles cannot be exactly predicted before a collision happens. The energy distribution in the quarks and gluons is estimated using parton distribution functions (PDFs). Interesting events are so-called "hard scatters" in which there is a large momentum transfer and the final state particles have high transverse momentum. This is in contrast to "minimum bias" events, in which little momentum transfer occurs and particles are deflected at only a slight angle to the beam line.

3.2 The ATLAS detector

ATLAS is one of two large general purpose detectors which will observe collisions at the LHC with the intent to observe the Higgs boson and discover new physics at the TeV scale. Made up of several sub-detectors, ATLAS aims to identify the particles produced in pp collisions and to measure their energy and momentum precisely. ATLAS has a cylindrical shape centred around the beam line and provides complete coverage in all directions except for directly down the beam line. The beam line is considered the z axis, with the x axis pointing into the centre of the LHC ring and the y axis pointing upwards. The angle ϕ defines location in the x-y plane from the x axis, and the polar angle θ is measured from the z-axis. Note that the ϕ and θ

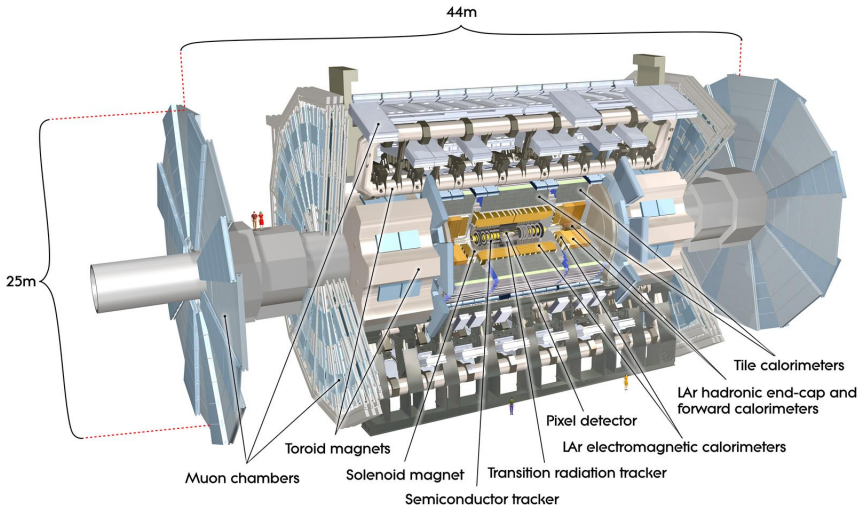

Figure 3.1: The ATLAS Detector. ATLAS Experiment © 2011 CERN.

described here are different than the angular variables discussed in Chapter 2. In general, the polar angle is expressed instead as pseudorapidity, defined as $\eta = -\ln(\tan\frac{\theta}{2})$ (see Figure 3.2). Pseudorapidity is used as a convenient scale since differences in η are invariant to Lorentz boosts along the beam axis, and minimum bias events have a charged track multiplicity that is roughly flat in η. Detector components such as calorimeter cells are therefore designed with a fixed value for $\Delta\eta$.

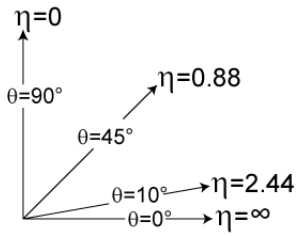

Figure 3.2: The pseudorapidity values corresponding to different polar angles.

3.2.1 Tracking

The innermost components of ATLAS are subdetectors designed to accurately measure the tracks of charged particles leaving the interaction point. The inner detector

is surrounded by a solenoid magnet which provides a 2 T magnetic field to curve the paths of charged particles. The detector is designed to have a high enough resolution to measure the sagitta of the curved tracks, which allows the momentum of a particle to be measured.

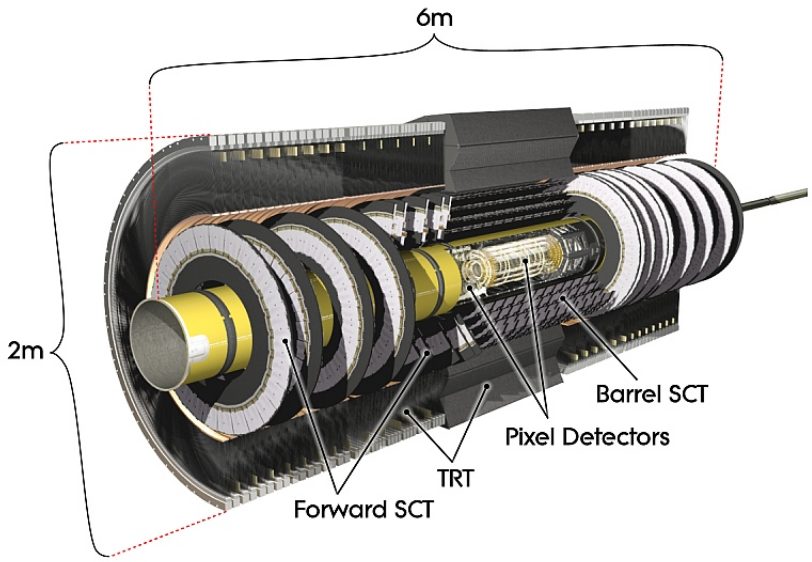

Figure 3.3: The ATLAS Inner Detector. ATLAS Experiment © 2011 CERN.

The greatest resolution is achieved by the silicon pixel detector, which is located 45.5-242 mm from the beam line and covers $|\eta| < 2.5$. The minimum pixel size is 50×400 μm. The pixel detector has three cylindrical layers and generally records 3 hits from a hard scattered particle, and has an intrinsic accuracy of 10 μm in the R-ϕ direction and 115 μm in z.

Outside the pixel detector is the semiconductor tracker (SCT), located at a radius 255 - 549 mm from the beam line. It consists of four cylindrical layers of silicon strips in the barrel, with nine disks on each endcap. Each layer consists of two sets of strips set at an angle of 40 mrad to each other in order to measure particle location in two dimensions, and generally eight layers record hits for each track. The SCT also covers

$|\eta| < 2.5$, and has an intrinsic accuracy of 17 μm (r-ϕ) and 580 μm (z).

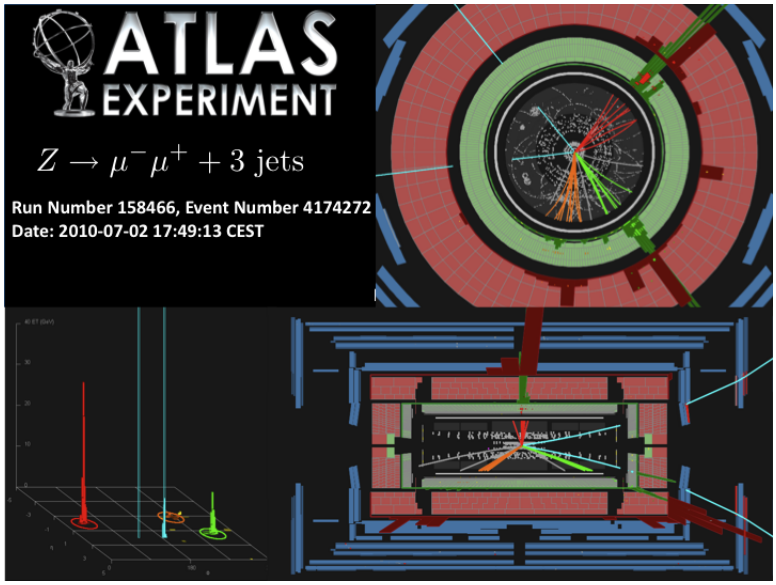

Figure 3.4: A sample $Z \rightarrow \mu\mu + 3$ jets event at ATLAS, shown in the ATLANTIS event display. ATLAS Experiment © 2011 CERN.

The outermost detector in the ID, located just inside the solenoid magnet, is the Transition Radiation Tracker (TRT). It is made up of straw tubes of 4 mm inner diameter, each of which is filled with an Xe (70%) CO_2 (27%) O_2 (3%) gas mixture and equipped with a gold-plated W-Re wire. The small diameter is required in order to collect all the electrons created by ionization from passing particles in the short time between bunch crossings. The detector discriminates between tracking hits, which must pass a low threshold, and transition radiation hits, which must pass a higher one. The transition radiation measurements are useful for particle identification. In the barrel the straws are located parallel to the beam line, while in the endcap they are positioned radially. Only R-ϕ information is obtained by the TRT, and it covers $|\eta| < 2$. Typically 30 hits are recorded per track, with an intrinsic accuracy of 130 μm. The tracks left by particles in the ID are useful for particle identification. In particular, photons, electrons and positrons all leave the same characteristic energy deposit in the electromagnetic calorimeter, and thus the presence of a track and its

curvature is a useful tool to differentiate them. The TRT also provides differentiation between electrons and pions, complementing information from the calorimeters.

3.2.2 Calorimetry

The ATLAS detector attempts to precisely measure the energy deposited in the detector after each collision. To do this, it relies on large calorimeters in the barrel and endcaps which stop most particles and measure the deposited energy. The electromagnetic calorimeter is located directly outside the solenoid magnet and is designed to absorb all of the energy from electrons, positrons and photons. Outside the EM calorimeter is the hadronic calorimeter, which stops all of the hadronic matter that passed through the EM calorimeter. Since this work does not discuss hadronic final states, the hadronic calorimeter will not be discussed in detail.

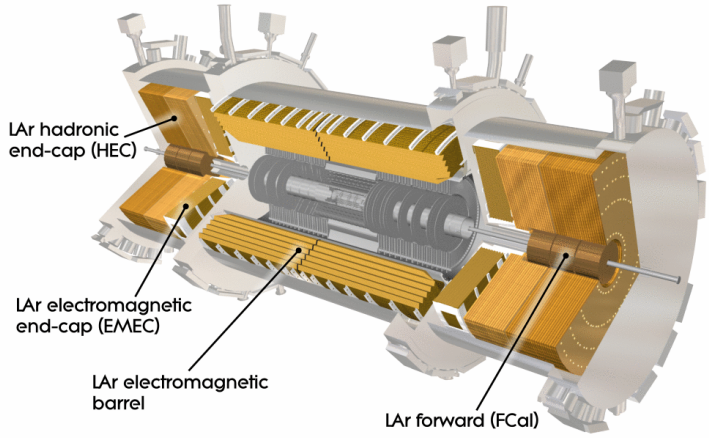

Figure 3.5: The ATLAS Calorimeters. ATLAS Experiment 2011 CERN.

For high momentum photons such as those produced in hard scatters, the dominant decay process in a material is pair-production. A photon passing through a medium will interact with the atomic electric fields, producing an electron positron

pair. These particles emit photons via bremsstrahlung radiation, which then also undergo pair production. In this method the original photon produces a shower of photons, electrons and positrons of lower energy until all of the energy has been absorbed by the calorimeter.

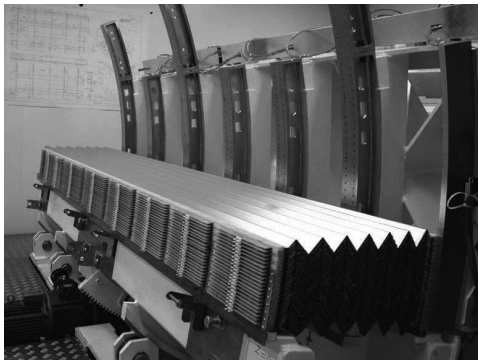

Figure 3.6: The partially constructed Liquid Argon calorimeter, showing the accordion structure [12].

High momentum electrons passing through matter lose their energy principally through bremsstrahlung radiation, which is the radiation released when the particle is slowed down by the nuclear magnetic fields of the matter through which it passes. The rate at which this radiation is emitted in a given medium is described by the radiation length, X_o. The radiation length of a material is the distance through which a beam of electrons must travel before its energy is reduced by a factor of e [13]. Electron energy loss by radiation is described by the formula

$$\left(\frac{dE}{dx}\right)_{\text{rad}} = -\frac{E}{X_o}. \tag{3.1}$$

As an electron enters the calorimeter and emits bremsstrahlung photons, the photons pair-produce and shower as described above. Thus photons and electrons shower in a similar manner in the calorimeter. They can be differentiated due to the fact that electrons leave tracks in the ID while photons pass through undetected, as well as the fact that photon showers tend to start deeper in the calorimeter. The mean distance

a shower travels in the calorimeter is given by

$$X = X_o \frac{\ln(E_o/E_c)}{\ln 2} \tag{3.2}$$

where E_c is the critical energy where ionization passes bremsstrahlung as the dominating mode of energy loss in the detector, and E_o is the energy of the initial particle.

The EM calorimeter is a sampling calorimeter, which means only part of it is sensitive to energy deposits, while the rest of the detector is inert. Both the barrel and endcap EM calorimeters use liquid argon (LAr) as the ionizing medium and lead plates as the absorber, and are arranged in an "accordion" geometry as shown in Figure 3.6. The purpose of the lead plates is to provide additional radiation lengths at low cost. The calorimeter measures the energy deposited in the liquid Argon and accounts for the energy deposited in the absorber. The barrel has a minimum thickness of 22 radiation lengths at $|\eta| = 0$ in order to capture the entirety of the EM showers [12].

3.2.3 Muon spectrometry

In the framework of ATLAS, muons are considered stable particles. Since heavier particles lose energy by ionization and bremsstrahlung at far smaller rates than lighter particles, high energy muons are able to pass through the EM and hadronic calorimeters without decaying. The muon spectrometer is therefore the outermost layer of the detector. The muon system consists of three cylindrical layers of drift chambers in the barrel and four large "wheels" of drift chambers on each endcap. In order to determine the momentum of the muons, there are three large toroidal magnets which curve the particle tracks. A barrel toroid and two endcap toroids produce toroidal magnetic fields of 0.5 T and 1 T, respectively. These fields allow momentum mea-

surements of muons between approximately 3 GeV and 3 TeV in the range $|\eta| < 2.7$. In order to obtain momentum resolution of approximately 10%, the resolution of the muon sagitta is measured to under 50 μm precision.

3.2.4 Trigger

Due to the high rate at which collision events occur in ATLAS, it is not possible to record all events to disk for offline analysis. An advanced trigger system is therefore necessary to distinguish which events should be written to disk and which should be ignored. The goal of the trigger system is to have maximal acceptance of interesting events while reducing the event rate to around 200 Hz.

The L1 trigger looks for general signatures of interesting events: high-p_T muons, photons and hadronic jets, as well as large missing transverse energy. Only certain parts of subdetectors which can respond quickly enough are used at this level, as the decision for each event must be made within 2.5 μs of the associated bunch crossing. The output rate of the L1 trigger is 75 kHz.

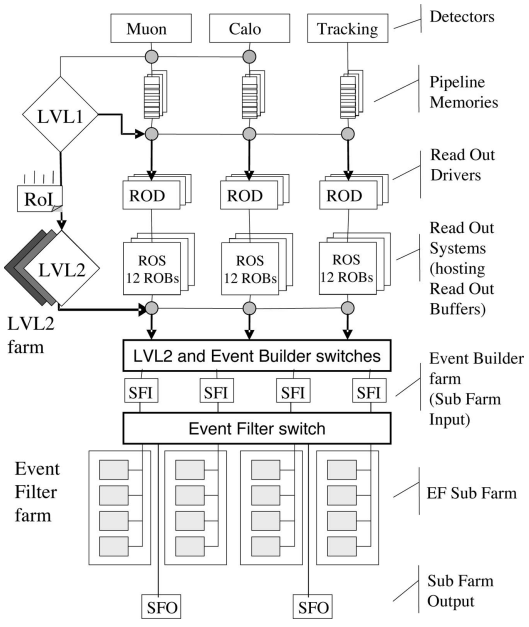

Figure 3.7: The ATLAS trigger system [14].

The L2 trigger uses the full granularity of the detector in the regions identified by the L1 trigger as Regions-of-Interest. The L2 trigger uses coordinates, energy and other signatures to further reduce the event rate to 3.5 kHz.

The Event Filter works offline and has 4 seconds to use fully-built events to reduce the event rate to approximately 200 Hz. The full resolution of the detector, as well as track reconstruction in the inner detector are available for making cuts.

Final states with high p_T leptons are extremely valuable for analysis due to the high resolution achieved in the EM calorimeter and the muon system, as well as the ability to eliminate much of the large QCD background in a pp collision. The $H \rightarrow ZZ^* \rightarrow 4l$ process is thus expected to have a high acceptance rate: approximately 85%, 92%, and 93% for the $2e2\mu$, $4e$, and 4μ channels respectively. The principle backgrounds which will not be eliminated at the trigger level are $gg \rightarrow ZZ \rightarrow 4l$, $Z(ee/\mu\mu)b\bar{b}$ and $t\bar{t}$, where the jets are mistaken for leptons during reconstruction.

Chapter 4

The ATLAS Monte Carlo

4.1 Overview

The ATLAS detector has recently begun to take data. In order to make predictions of how well the experiment will be able to distinguish differing Higgs signals, this work relies principally on simulated events. Monte Carlo (MC) production methods make it possible to simulate the way particles behave in pp collisions and to imitate the way the detector will record real data. In this way it is possible to compare the effects that different theories would have on the actual observations made by the detector. Broadly, producing ATLAS MC samples consists of three main steps: Event generation, where particle production and decay is modelled according to theory; Simulation/Digitization, where the generated particles interact with a computer model of the detector, producing events similar to the data produced by the actual detector; and Reconstruction, where the simulated events are turned into physics objects which can be analyzed by users. The reconstruction process is identical between simulated events and real data.

4.2 Event Generation

Event generation for this study was performed using the PYTHIA generator [15]. PYTHIA is a multi-purpose lowest order event generator commonly used in particle physics. Lowest order in this case means that the matrix elements of physics processes are only calculated to the lowest non trivial order in perturbation theory. Higher order processes such as quark loops are ignored. Final state quantum electrodynamic radiation is modelled by the program PHOTOS [16]. PYTHIA models initial state protons as a collection of on-shell quarks, off-shell quarks and gluons, whose momenta are modelled by CTEQ parton distribution functions (PDFs) [17]. Interactions between constituent particles then proceed according to the Standard Model, or a specified non-Standard Model theory.

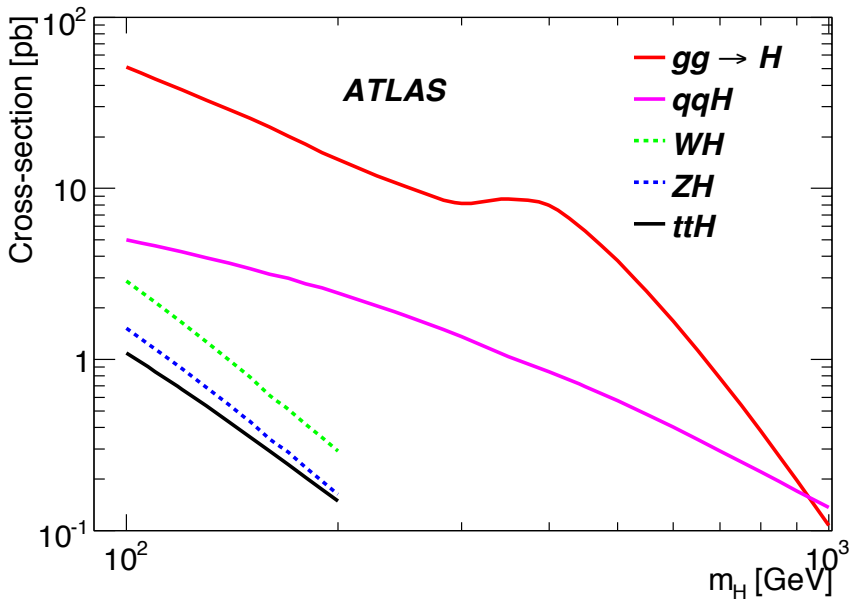

Figure 4.1: Anticipated production cross-sections of the Higgs boson at ATLAS, at 14 TeV. ATLAS Experiment © 2011 CERN.

This study uses inclusive Higgs production, which includes all mechanisms for producing a Higgs boson. As the true Higgs mass is as yet unknown, 140 GeV was

chosen as a nominal value. As shown in Figure 4.1, the dominating mechanism for this process is gluon-gluon fusion (ggF), where a Higgs boson is produced through a top quark loop. The secondary production measurement is vector boson fusion (VBF). The contributions of each process to the total production cross-section are shown in Table 4.1. In this process two quarks each emit either a Z^0 or $W^{\pm}$, which interact with each other to produce a Higgs. The final state of this process includes two jets. In the case of a $W^{\pm}$ interaction, the jets will have a different flavour than the original interacting quarks. VBF has a cross-section approximately one tenth as large as ggF. The remaining production mechanisms are associated production mechanisms, and have comparatively small cross-sections. In these processes, a Higgs boson is radiated by either a Z^0, $W^{\pm}$, or top quark (or anti-top quark) created through any other process.

Once produced, the Higgs particle in each event is forced to decay to two Z bosons, one of which is off shell. The Z bosons are then forced to decay into either e^+e^- or $\mu^+\mu^-$ pairs. There is an even chance of either decay, so the $e^+e^-e^+e^-$ and $\mu^+\mu^-\mu^+\mu^-$ final states each happen approximately 25% of the time, while the mixed final state $e^+e^-\mu^+\mu^-$ occurs about half the time. The branching ratio for $H \to 4l$ is 0.0003159 [12], and so the cross-section for this process is $\sigma_{H\to 4l} = 0.01501$ pb for $\sqrt{s} = 14$ TeV.

4.3 Simulation

Simulation is the most computationally intensive portion of the MC process. The particles generated by PYTHIA are run through a detailed computer model of the ATLAS detector in GEANT4 [19]. The model contains material and density information for the full three-dimensional detector. This process simulates the way each individual particle created by PYTHIA would interact with the matter of the real

Production Mode	σ [pb]	PDF [%]	scale [%]
ggF	41.70	$^{+3.7}_{-2.8}$	$^{+7.9}_{-8.5}$
VBF	3.657	$^{+2.4}_{-2.4}$	$^{+3.2}_{-2.4}$
WH	1.122	$^{+1.57}_{-1.37}$	$^{+0.07}_{-0.00}$
ZH	0.659	$^{+1.43}_{-1.20}$	$^{+2.00}_{-1.25}$
$t\bar{t}H$	0.404	$^{+1.61}_{-2.53}$	$^{+35.1}_{-23.9}$
Total	47.542		

Table 4.1: NLO cross-sections for Higgs production mechanisms at $\sqrt{s} = 14$ TeV and $M_H = 140$ GeV. Scale uncertainties result from missing higher order corrections. PDF uncertainties results from CTEQ PDF fit [18].

detector. The interaction of the particles with the detector and the magnetic fields are simulated and sampled in 25 ns steps, the same rate as in the real detector. Hits in the inner detector, showers in the calorimeter, and hits in the muon chamber are created in this stage and are saved to files called Raw Data Objects (RDOs), which are the same data type created by the detector.

4.4 Reconstruction

Reconstruction is the process of turning energy deposits in the detector into physics objects which can be analyzed by scientists. The same process is used for data and simulated events. Several algorithms are used to calculate quantities relevant for analysis. These algorithms can be subdetector specific, such as turning hits in the inner detector into tracks. They can also rely on multiple parts of the detector, such as calculating the missing transverse energy of an event or the 4-momentum of a particle.

There are two types of output files: Event Summary Data (ESDs) and Analysis Object Data (AODs). An ESD contains the detector level information of each event such as tracks and hits in the detector, as well as physics objects. An AOD contains only physics objects such as electrons, jets and missing E_T. The purpose of this distinction is to have the ESDs contain all potentially relevant information about an event, while the smaller AODs can be distributed widely and used for analysis. The work in this study was performed on user-created AODs.

4.5 Monte Carlo Event Samples

The event samples used for this study are based on the event sample MC8.109065.PythiaH140zz4l, created by official ATLAS MC production. This sample was used as the baseline for Standard Model events. In order to create samples with non-SM HZZ couplings, the PYTHIA routine governing the decay was modified so that the angular distributions are parametrized according to equation 2.1 [20]. MC event samples were then produced for coefficients (0,1,0), (0,0,1) and (1,0,1), and are listed in Table 4.2.

Event Sample		Available Events
$H \to ZZ \to 4l$	(1,0,0)	29680
	(0,0,1)	27150
	(0,1,0)	28600
	(1,0,1)	27700
$ZZ \to 4l$		194676
$t\bar{t}$		41495
$Zb\bar{b}$		50342

Table 4.2: Signal MC event samples, produced with $M_H = 140$ GeV.

The principle background for this study is the $gg \to ZZ \to 4l$ decay. When the invariant mass of the 4 leptons occurs in the range around m_H, this background is irreducible as it has the same experimental signature as the signal process. Other

backgrounds are due to QCD jets faking leptons. This occurs when a jet is falsely reconstructed as an electron or a muon. Hadrons created during showers in the hadronic calorimeter can also punch through the calorimeter, creating hits in the muon system. Thirdly, leptons can be created in jets or hadronic showers and falsely identified as coming from the primary vertex. The processes which are vulnerable to these effects are primarily $t\bar{t}$ and $Zb\bar{b}$ decays.

Chapter 5

Event Selection and Analysis

5.1 Lepton Identification and Acceptance

5.1.1 Electron ID

Electron identification begins during online event processing. Electrons are identified as electromagnetic (EM) objects, which can be either electrons or photons. EM objects are characterized by showers which deposit at least 30% of their energy in the second layer of the EM calorimeter. Shower energy and radius, among other variables, are also taken into account [22]. EM objects suspected to be electrons fall into one of three categories: Loose, Medium or Tight. The loose category is based only on shower shape and the selection criteria are common to both photons and electrons. Medium electrons require track information from the inner detector to be matched to a shower. Tight electrons require more stringent track matching as well as additional particle identification information from the TRT. Tracks are reconstructed by following the particle hits from the interaction point to the beginning of the shower in the calorimeter. Electrons are differentiated from positrons by the curvature of the track due to the influence of the solenoid magnet's field. Tracks from

negatively charged particles curve in the positive ϕ direction, while positive tracks curve the opposite way. Loose identification efficiently selects real electrons, at the expense of background fake electrons. Conversely, tight identification is less efficient in selecting real electrons, but provides greater rejection of jet background. The efficiencies and jet rejection factors of each type of electron type are listen in Table 5.1, and the efficiencies are plotted against transverse energy and pseudorapidity in Figure 5.1. Since further cuts are applied in this study to remove jet backgrounds, medium electron identification is used in order to achieve maximal electron acceptance.

Cuts	Efficiency (%)	Rejection factor
Loose	87.97	567
Medium	77.29	2184
Tight	64.22	9.9×10^4

Table 5.1: Efficiencies and jet rejection factors for Loose, Medium and Tight electrons [1].

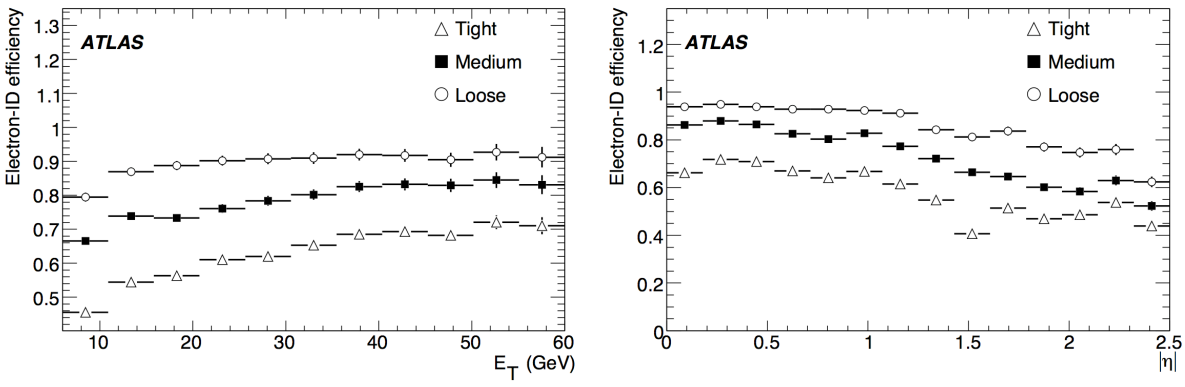

(a) (b)

Figure 5.1: Acceptance efficiencies for Loose, Medium and Tight electrons from $H \rightarrow eeee$ decays [1].

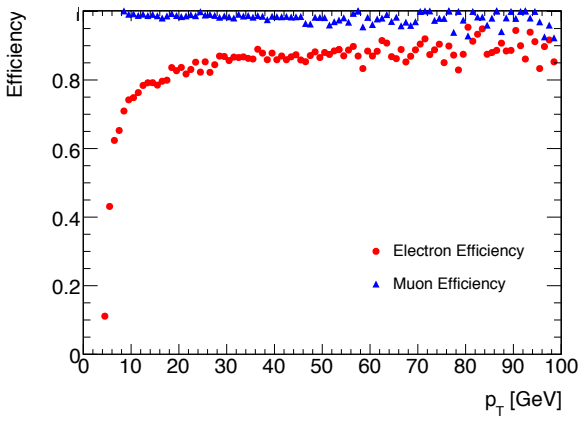

Figure 5.2: Acceptance efficiencies for final state leptons from signal events in the event samples used for this analysis.

5.1.2 Muon ID

Muon identification is considerably less ambiguous than electron identification. Radiative energy loss scales with m^{-4}, therefore unlike electrons, muons pass through the calorimeter system relatively unaffected. The calorimeters are designed to be thick enough to stop all other known particles (excluding neutrinos, which do not deposit energy in the detector) from reaching the muon system. Muons can be identified by tracks in the muon system which extrapolate back to the beam line. Most cosmic muons can be identified by a large impact parameter – the closest distance between the extrapolated track and the interaction point. Cosmic muons which pass close to the interaction point are identified by measuring the time difference between the hits in either side of the muon system, to differentiate between two back-to-back muons originating near the primary vertex. There are three classification types for reconstructed muons: "Combined muons" are reconstructed from hits in the muon system, extrapolated back to the primary vertex, and matched with an inner detector track; "Extrapolated muons" have hits in the muon chamber but do not need to be matched to an inner detector track; "Low-p_T" muons are reconstructed in the inner detector and matched to hits in the muon detector not associated with either of the

above types. The latter method is effective for muons with $p_T < 10$ GeV. ATLAS supports two algorithms for each type of muon, which are grouped into either the Staco [21] or Muid families. This analysis uses the Staco family of algorithms for muon identification, as it is currently the default for physics analysis at ATLAS. The efficiencies of the electron and muon reconstruction in the event samples used for this study are shown in Figure 5.2.

5.1.3 Trigger Acceptance

During the reconstruction portion of the Monte Carlo process, the full trigger chain is simulated. The resulting AODs contain information on the frequency at which events passed given filters. The acceptance efficiencies for selected triggers are listed in Table 5.2. The triggers are classified by the type of lepton as well as the energy needed for the trigger to accept the event (for example, the $2e10$ trigger requires 2 EM objects with $E_T \geq 10$ GeV). It is clear that acceptances greater than 90% are achievable in all channels by using the 10 GeV triggers. As the luminosity of the LHC increases, it may become necessary to prescale these triggers. At some point (depending on the amount of prescaling) it would be optimal to switch to the 20 GeV triggers, which would be scaled by a smaller amount, if at all. This study will assume the use of the 10 GeV triggers.

5.2 Event Selection and Background Reduction

In order to optimize signal acceptance and minimize backgrounds, offline data cuts must be performed on events which pass the online triggers and are written to disk. Events are preselected to have at least 4 loose leptons, with $|\eta| < 2.5$ and $p_T > 5$ GeV. These cuts are required to ensure that the leptons are in the area of maximum coverage

Trigger Menu	Generated Sample					
	4e	4mu	2e2mu	Inclusive Signal	ZZ	$t\bar{t}$
mu10	0.0013	0.963	0.849	0.689	0.259	0.259
mu20	0	0.889	0.675	0.583	0.425	0.182
e10	0.942	0.0092	0.844	0.701	0.497	0.154
e20	0.915	0.0086	0.831	0.634	0.690	0.197
mu10 AND e10	0.0013	0.009	0.729	0.408	0.214	0.195
mu10 OR e10	0.943	0.963	0.954	0.982	0.788	0.259
mu20 AND e20	0	0.009	0.493	0.273	0.165	0.116
mu20 OR e20	0	0.889	0.675	0.583	0.425	0.182

Table 5.2: Selection efficiencies for various trigger menus.

of the detector and that they have high enough momentum for accurate measurement. Further cuts are then performed to ensure that at least two leptons have $p_T > 20$ GeV, with the remaining two leptons having $p_T > 7$ GeV [1].

5.2.1 Lepton Isolation

Calometric and track isolation requirements are also used to extract signal events. Leptons from Z boson decays should be isolated; that is, they should be isolated from other activity in the event such as hadronic decays. Leptons created in hadronic jets are expected to be surrounded by other particles in the same shower. In order to differentiate between these cases, a cone is defined around each lepton in the eta-phi plane, such that the radius of the cone is $\Delta R = \sqrt{\Delta\eta^2 + \Delta\phi^2} > 0.2$. A discriminant is calculated by summing the transverse energy of the particles inside the cone but excluding the energy of the lepton, and then normalizing by the lepton transverse energy. The isolation discriminant distributions for electron and muon events are shown in Figure 5.3. An isolated lepton should have a smaller discriminant than a lepton from a hadronic decay. For this work, the selection cut for the isolation discriminant was chosen to be 0.15 [3].

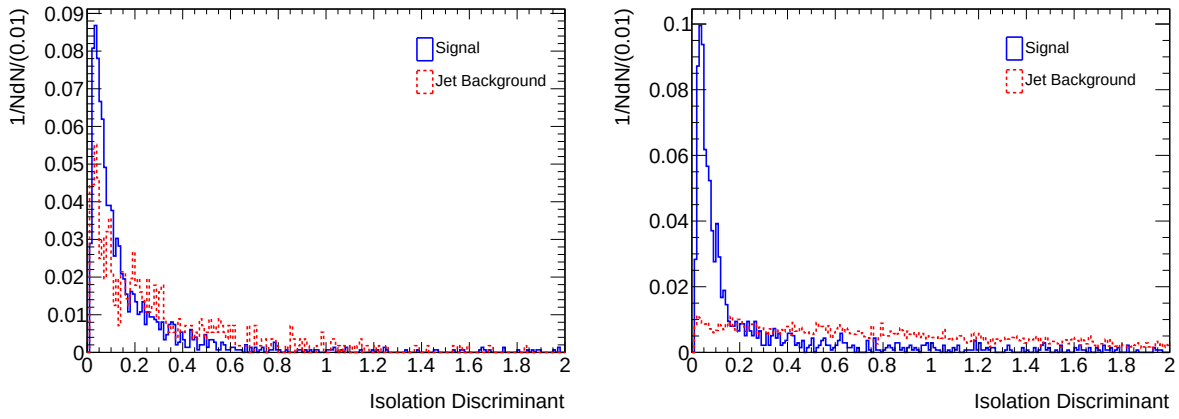

(a) Electron sample (b) Muon Sample

Figure 5.3: Lepton isolation discriminant distribution for signal and jet background samples. This analysis requires the discriminant to be less than 0.15 [3]

5.2.2 Impact Parameter

The impact parameter (d_0) of a final state lepton is defined as the distance of closest approach of the reconstructed track to the interaction point. This is a relevant quantity for analysis because it allows one to distinguish between particles which originate from the main vertex or from displaced vertices. In signal events, the Higgs and Z bosons will decay promptly, so final state leptons will appear to originate from the interaction point. Leptons from $t\bar{t}$ and $Zb\bar{b}$ events will originate from displaced vertices, due to the longer lifetime of the b quark ($c\tau = 491.1\ \mu m$). Decays from the $ZZ \rightarrow 4l$ background are prompt, and will not be reduced by an impact parameter cut. The impact parameter has more power in identifying muon final states since bremsstrahlung radiation smears the d_0 distribution for electrons. The position of the primary vertex is measured using the tracks of particles in the inner detector, and a vertex fit is also applied to the four signal leptons. The d_0 significance (Sd_0) is determined by calculating the minimum χ^2 value for the common vertex hypothesis. These distributions are shown in Figure 5.4. A larger Sd_0 implies that the four leptons do not originate at the interaction point. For muons, Sd_0 is required to be less

than 3.5, and for electrons less than 6.

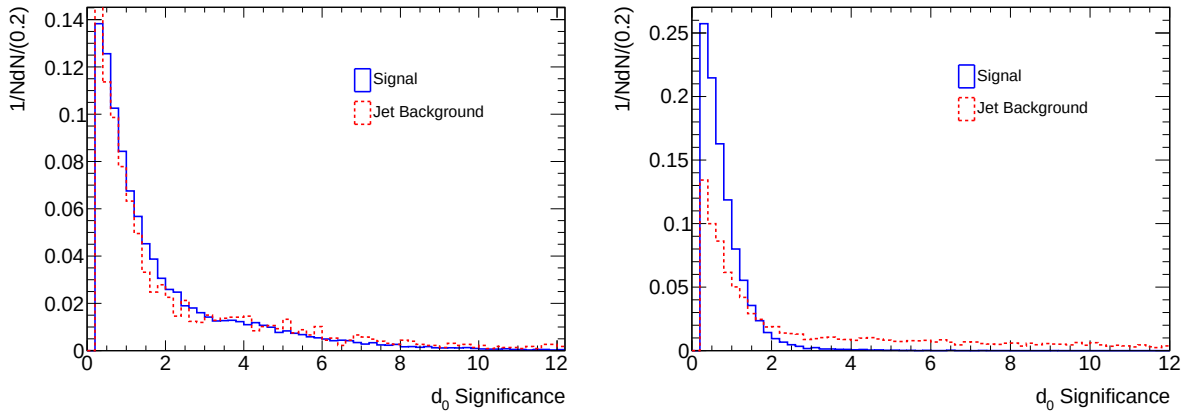

(a) Electron sample (b) Muon sample

Figure 5.4: Impact parameter significance distribution for signal and background events. This analysis requires Sd_0 less than 3.5 and 6 for muons and electrons, respectively.

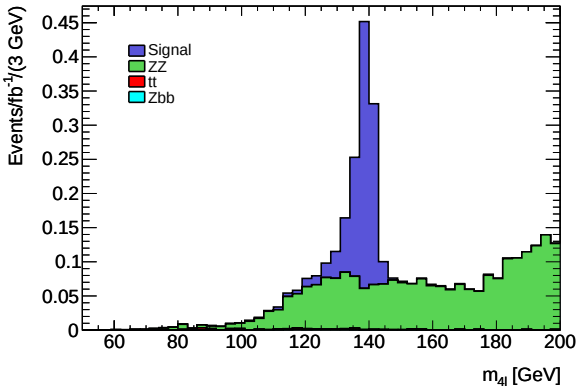

Figure 5.5: Reconstructed 4-lepton mass for signal and background processes, for a 140 GeV Higgs boson.

5.2.3 Kinematic Requirements

Should at least four leptons in an event pass all of the above cuts, the masses of possible Z bosons are reconstructed according to the equation $M_Z = \sqrt{(E_i + E_j)^2 - (p_i + p_j)^2}$. The Z candidate with a reconstructed mass closest to the nominal Z mass ($M_Z =$

91.19 GeV) is labeled Z_1, and the second candidate is labeled Z_2. If there are more than 2 possible Z candidates, Z_1 remains the candidate whose mass is closest to the nominal Z mass, and Z_2 is the remaining candidate whose daughter leptons have the highest p_T.

The Higgs mass is reconstructed from the energy and momentum of the Z candidates, as above. Kinematic constraints can be placed on both the Z boson and Higgs candidates in order to further reduce background. In this analysis, the requirements are imposed for M_{Z_1} to be within $\pm$15 GeV of the nominal Z mass, and for $M_{Z_2} > 20$ GeV. It is also required that M_H is within $\pm$ 15 GeV of the nominal Higgs mass, 140 GeV in this analysis. This restriction has little effect on signal events due to the narrow distribution of the Higgs mass in this mass range, and so is an effective cut to reduce the ZZ background. Table 5.3 shows the cut flow efficiencies for signal and background events. The four lepton invariant mass for signal and background processes is shown in Figure 5.5. All selection cuts have been applied, as well as the Z mass constraint, but not the Higgs mass constraint in order to show the ZZ background. The cross-sections for each process after all data cuts and kinematic constraints are shown in Table 5.4.

Cut	Efficiency			
	$H \to 4l$	$ZZ \to 4l$	$t\bar{t}$	$Zb\bar{b}$
Trigger	0.953	0.788	0.259	0.914
Preselection, Geometric acceptance, p_T	0.401	0.305	0.0014	0.024
Isolation Cut	0.287	0.195	$8.2 \cdot 10^{-4}$	0.011
Impact Parameter Cut	0.246	0.144	$2.6 \cdot 10^{-4}$	0.0085
Z mass window	0.223	0.121	$8.8 \cdot 10^{-5}$	0.0011
H mass window	0.213	0.058	$3.6 \cdot 10^{-6}$	$1.2 \cdot 10^{-5}$

Table 5.3: Cut flow efficiency of signal and background samples.

Process	Cross-Section (fb)
Signal	3.197
ZZ	0.491
$Zb\bar{b}$	0.0823
$t\bar{t}$	0.0542

Table 5.4: Signal and background cross-sections after event selection, in fb for 14 TeV collisions.

5.3 Analysis

5.3.1 Performing Pseudo-Experiments

Several observables will be accessible to the ATLAS detector for analysis in order to determine the sensitivity of the detector to the CP structure of the Higgs sector. As discussed in Chapter 2, these observables are the angular distributions ϕ and $\cos\theta$. Using the simulation procedures discussed in Chapter 4, simulated experiments were performed by creating sets of signal and background events corresponding to integrated luminosities of 10, 50 and 100 fb^{-1}. The number of events needed for each luminosity category was shown in Chapter 4. The observables were measured from the simulated events and binned into histograms. As a compromise between having enough events in each bin to have reasonable errors, and having enough bins to accurately discern the shape of the distribution, the number of bins in each histogram was chosen to be 12. Figures 5.6 and 5.7 show the observables ϕ and $\cos\theta$, respectively, for a sample simulated experiment with 100 fb^{-1} of luminosity. The points with error bars represent the data-like histograms, while the bar histograms represent the normalized reference histograms made using the entire event sample for each coupling type.

In Figures 5.8 and 5.9, ZZ background, shown in blue, is added to the signal histogram to more accurately reflect real conditions. The reference histograms are again scaled to include the added events. In order to identify useful test statistics,

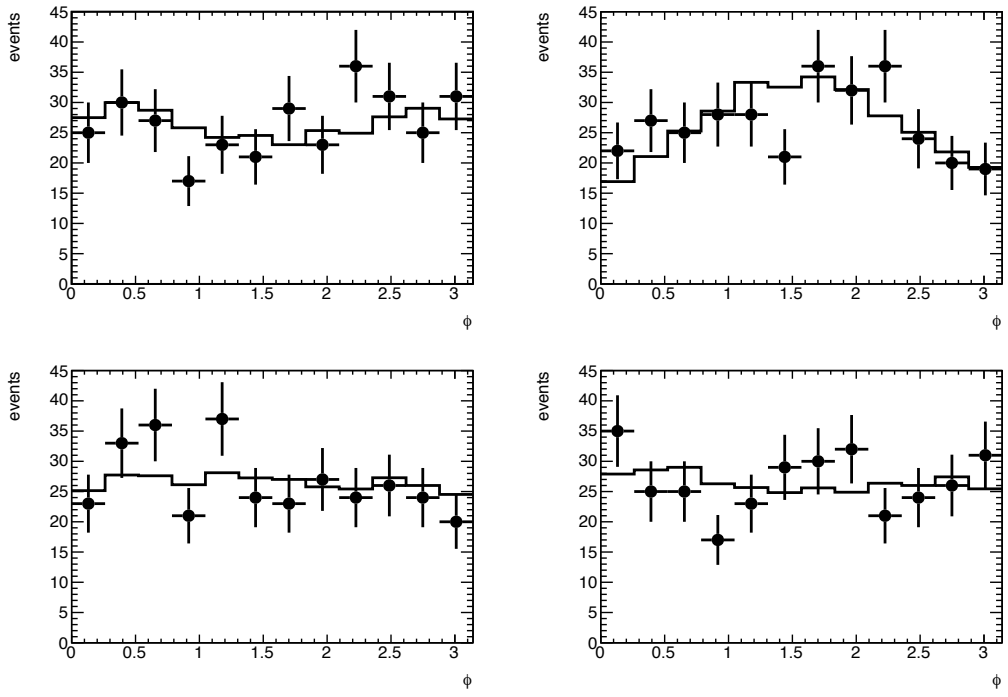

Figure 5.6: Example simulated events superimposed on reference histogram scaled to 100 fb^{-1} for the four different coupling types. Clockwise from top left: Standard Model, CP Odd, CPV, CP Even.

and to estimate probability distribution functions for them, the simulated experiment was repeated 1000 times using different signal and background events.

5.3.2 ZZ Background

Before analysing the signal distributions, the shape of the ZZ background must be considered. By taking the entire ZZ simulated event sample and calculating the observables ϕ and $\cos\theta$ for each event, any systematic trends in the background should be apparent. These distributions can be seen in Figure 5.10. In fact, slight periodic features can be seen in both observables. There is also noticeable asymmetry in the distributions, particularly in ϕ. The asymmetry can be quantified as

$$A_\phi = \frac{\Gamma(\phi < \pi/2) - \Gamma(\phi > \pi/2)}{\Gamma(\phi < \pi/2) + \Gamma(\phi > \pi/2)} \tag{5.1}$$

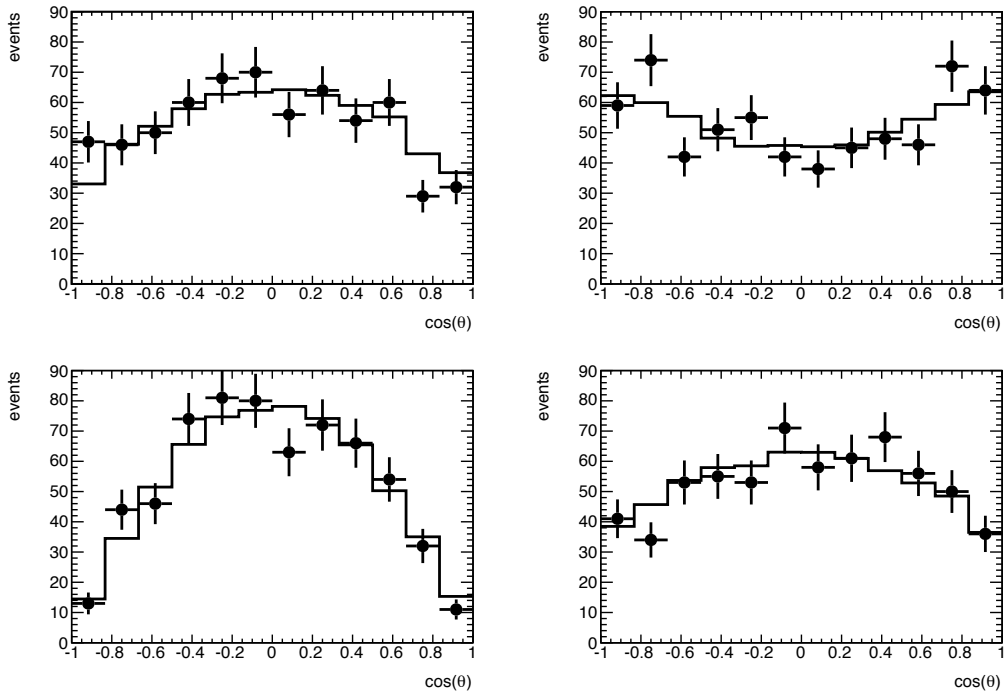

Figure 5.7: Example simulated events superimposed on reference histogram scaled to 100 fb^{-1} for the four different coupling types. Clockwise from top left: Standard Model, CP Odd, CPV, CP Even.

and

$$A_{\cos\theta} = \frac{\Gamma(\cos\theta < 0) - \Gamma(\cos\theta > 0)}{\Gamma(\cos\theta < 0) + \Gamma(\cos\theta > 0)} \tag{5.2}$$

for the two distributions. The fits and asymmetries in the background distribution are shown in Table 5.5.

	Fit equation	$\chi^2_{fit}/12$	$\lvert A\rvert$
ϕ	$-117\phi^4 + 751\phi^3 - 1467\phi^2 + 911\phi + 2964$	9.17/12	0.012
$\cos\theta$	$-1395\cos^4\theta - 124\cos^3\theta + 992\cos^2\theta + 73\cos\theta + 6146$	30.92/12	0.0028

Table 5.5: Fourth order polynomial fit, and its χ^2 value, for each angular distribution, along with their asymmetry.

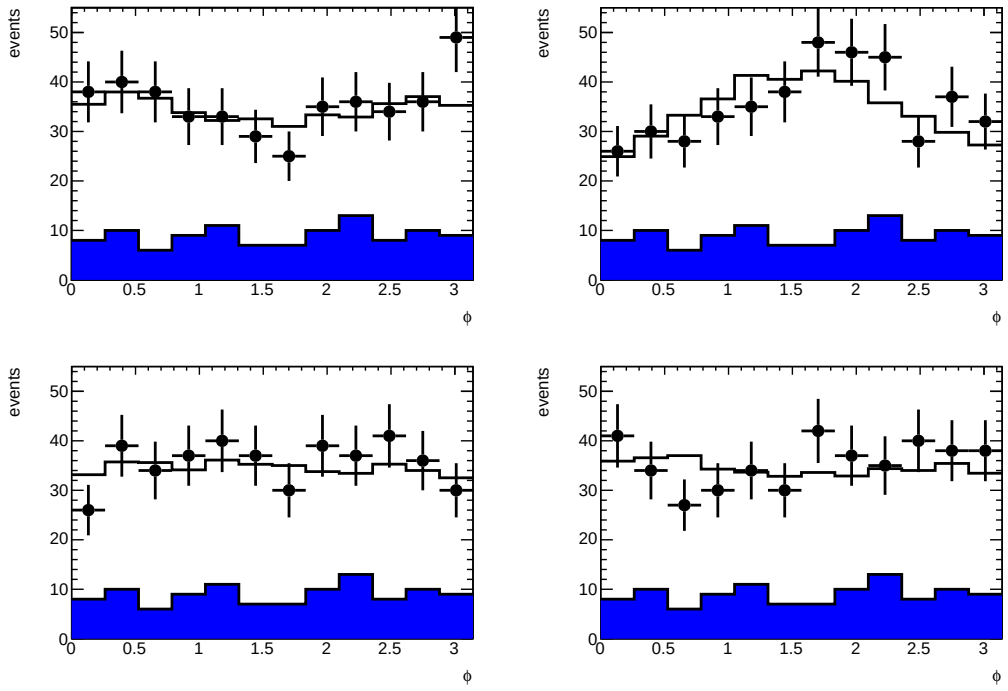

Figure 5.8: Example simulated events superimposed on reference histogram scaled to 100 fb^{-1} for the four different coupling types. The ZZ background is added to the signal histogram, and is shown overlayed in blue. Clockwise from top left: Standard Model, CP Odd, CPV, CP Even.

5.3.3 Direct Comparison

The first technique used to identify Higgs CP structure was a direct comparison between the data-like histograms of ϕ and $\cos\theta_i$ and the reference histograms for each coupling type. Since the distributions for $\cos\theta_1$ and $\cos\theta_2$ are identical in all cases, they can be binned together as a single observable, $\cos\theta$. $\cos\theta_i$ histograms therefore have twice the statistics as ϕ histograms. A χ^2 test performed between simulated and reference histograms would have 12 degrees of freedom, one for each bin in the histogram. Assuming that the uncertainty in the signal histogram is Gaussian and binwise independent, the χ^2 distribution of the 1000 experiments, when comparing histograms of the same coupling type, should peak at 12 with a narrow distribution. Comparing unlike histograms should produce χ^2 values with a wider distribution, cen-

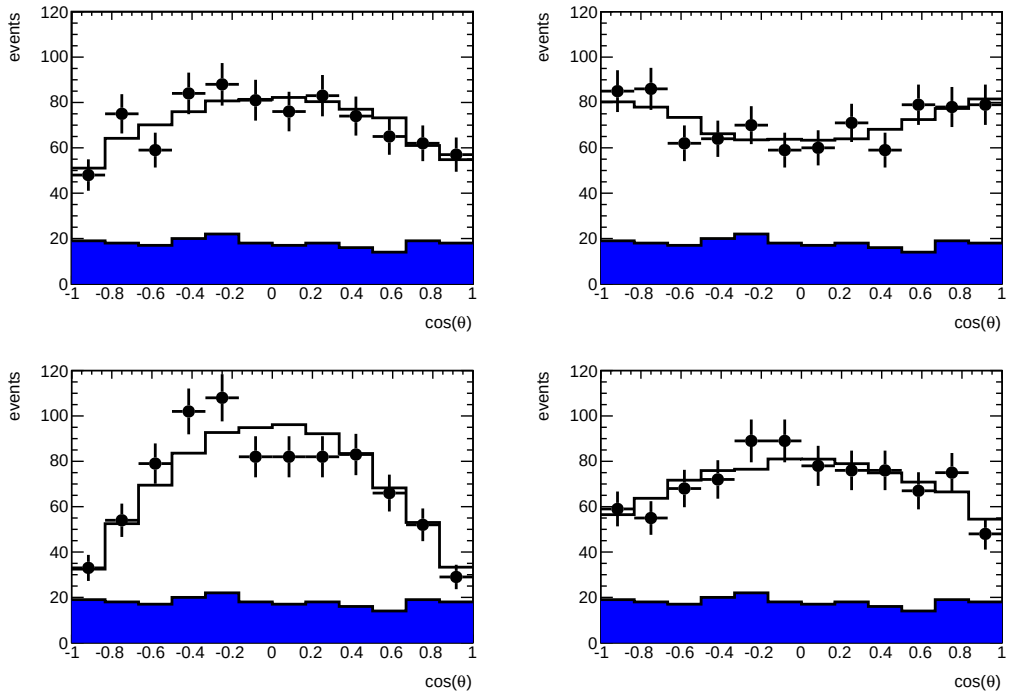

Figure 5.9: Example simulated events superimposed on reference histogram scaled to 100 fb^{-1} for the four different coupling types. The ZZ background is added to the signal histogram, and is shown overlayed in blue. Clockwise from top left: Standard Model, CP Odd, CPV, CP Even.

tred at a value greater than 12. Histograms peaking well below 12 would imply that the error bars and the histograms (which are purely statistical) do not represent the true uncertainty in the data. The ability of this test to discriminate between hypotheses is determined by the separation between the various χ^2 distributions associated with each reference histogram.

Figures 5.11 and 5.12 show the χ^2 distributions for ϕ and $\cos\theta$, respectively. The four plots in each Figure show the χ^2 distributions for each of the four coupling types being compared to a single reference histogram. The black, solid histogram corresponds to the distribution where the reference is being compared to samples of the same type. The other three histograms in each plot correspond to the same reference histogram being compared to the other three coupling types.

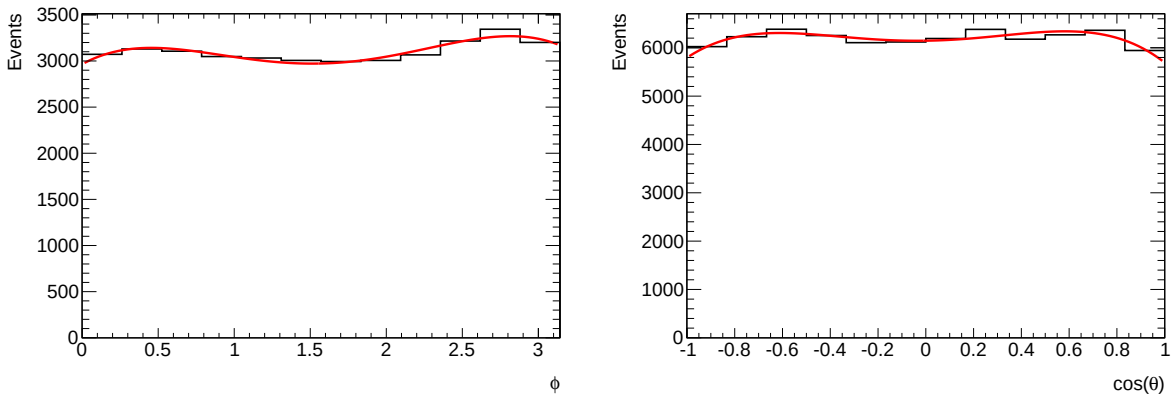

Figure 5.10: Angular distributions of entire irreducible background event sample, with 4th order polynomial fit.

When enough real events are available to investigate Higgs properties directly, the observables will be measured, binned, and compared to each reference histogram. In each of the four statistical tests, the null hypothesis (H_0) is that the measured distributions are consistent with the reference histogram. The ability to test each null hypothesis against the alternatives is described by two numbers. The significance level, a, is the probability of a statistical fluctuation causing the test to erroneously reject H_0 (known as a type-I error). The area to the left of a is the region in which H_0 is accepted, and to the right is rejected. The alternate hypotheses are also taken into account through a quantity called the power of the test. Power is defined as 1-b, where b is the probability of accepting the null hypothesis given that the alternate hypothesis is true (a type-II error). In Figures 5.11 and 5.12, the black arrow represents the location of the cutoff corresponding to $a = 0.01$. Tables 5.6, 5.7 and 5.8 show the power of each possible test for the given test significance.

It is immediately apparent, both by inspecting the χ^2 distributions and looking at the powers of the hypothesis tests that the $\cos\theta$ observable has a much greater discriminating power than ϕ. Using only $\cos\theta$, and requiring a significance of 0.01 and a power 0.9 at 100 fb^{-1}, it is possible to differentiate between all combinations

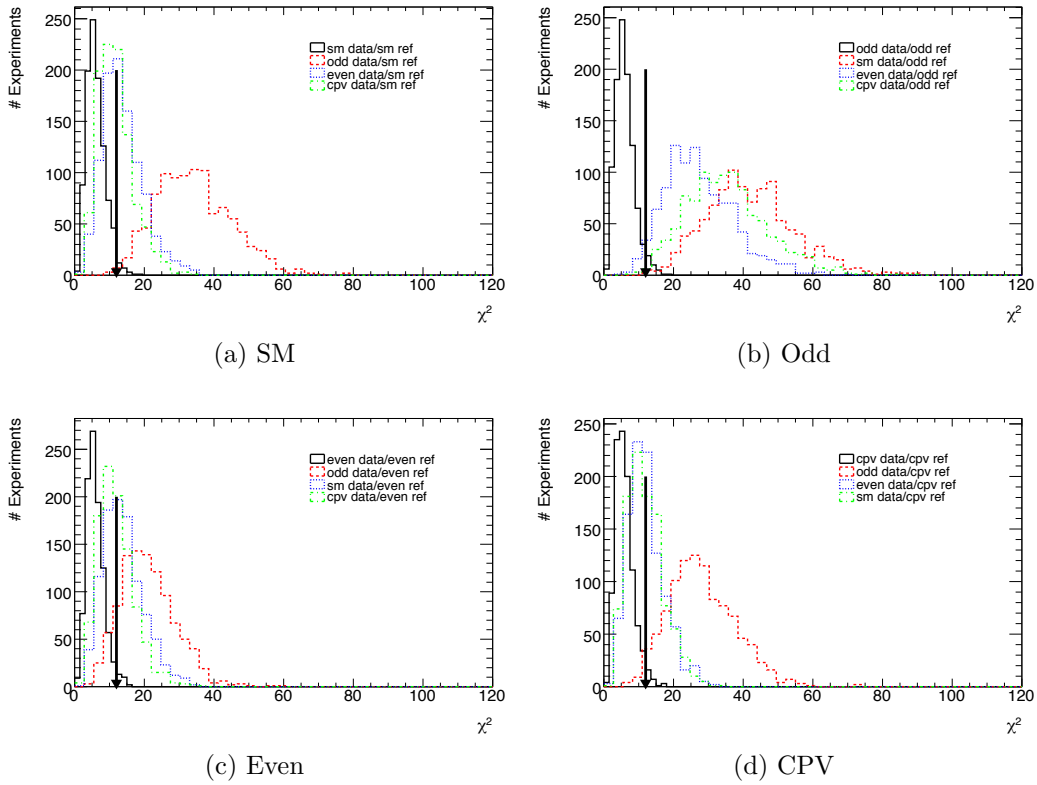

(a) SM (b) Odd

(c) Even (d) CPV

Figure 5.11: χ^2 distributions when comparing ϕ data-like histograms of the 4 coupling types to each reference histogram, with 100 fb^{-1} of luminosity. In each figure, the solid black histogram corresponds to the distribution where the reference is being compared to the sample of the same type (null hypothesis), while the other lines correspond to samples of the 3 different types. The arrow corresponds to a significance level of 0.01 for the null hypothesis.

of coupling types except for SM and CPV, which create similar χ^2 distributions. At 50 fb^{-1} the ability to exclude the CP-even model is also lost given Standard Model coupling, but all other tests remain viable. With 10 fb^{-1}, all discriminating power is lost. This method of discriminating between the various hypotheses can therefore be considered reliable with large amounts of data.

It is worth examining whether combining the two observables will improve the power of this test. To do this, a Fisher discriminant analysis is used. To perform the Fisher analysis, it is assumed that it is possible to create a new test statistic

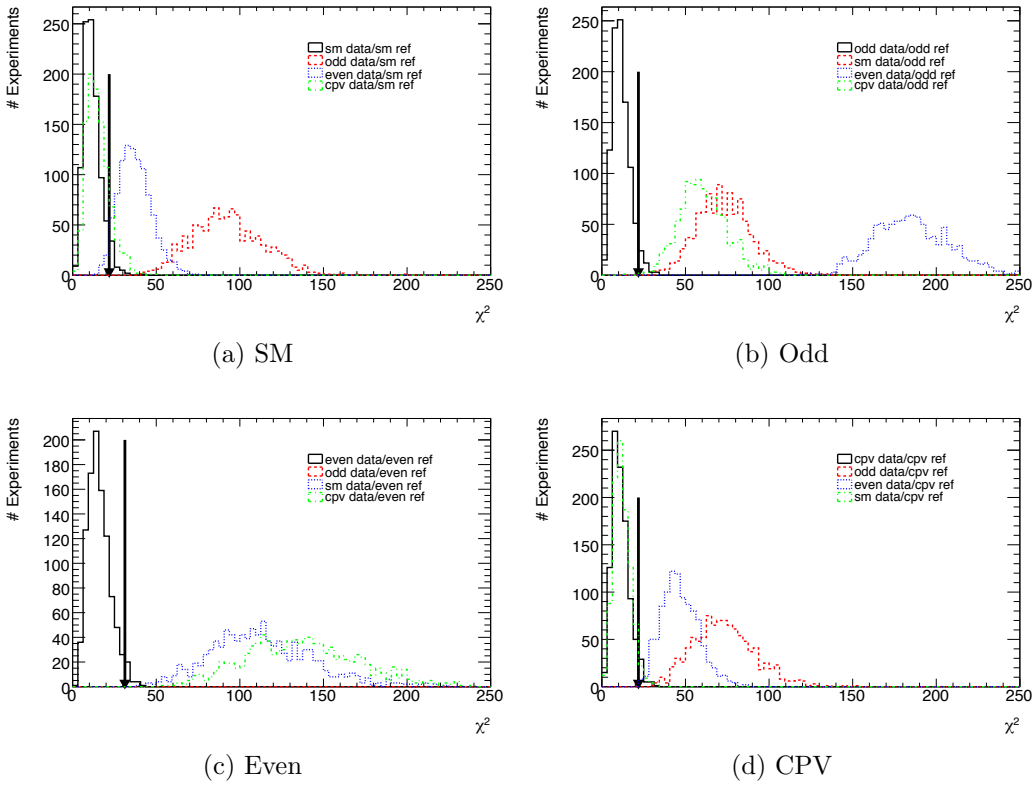

(a) SM (b) Odd

(c) Even (d) CPV

Figure 5.12: χ^2 distributions when comparing $\cos\theta$ data-like histograms of the 4 coupling types to each reference histogram, with 100 fb^{-1} of luminosity. In each Figure, the solid black histogram corresponds to the distribution where the reference is being compared to the sample of the same type (null hypothesis), while the other lines correspond to samples of the 3 different types. The arrow corresponds to a significance level of 0.01 for the null hypothesis.

$t_\chi(\phi, \cos\theta)$ that is a function of both test statistics, such that

$$t_\chi(\chi^2_\phi, \chi^2_{\cos\theta}) = a_1 * \chi^2_\phi + a_2 * \chi^2_{cos\theta}. \tag{5.3}$$

The coefficients a_i are calculated so that difference in the means of H_0 and H_1 is maximized for each test via the equation

$$\vec{a} \propto W^{-1}(\vec{\mu_0} - \vec{\mu_1}), \tag{5.4}$$

Reference	ϕ				$\cos\theta$			
	SM	Odd	Even	CPV	SM	Odd	Even	CPV
SM	X	0.805	0.0509	0.0189	X	0.999	0.912	0.0879
Odd	0.923	X	0.562	0.809	0.999	X	0.999	0.997
Even	0.045	0.289	X	0.024	0.999	0.999	X	0.999
CPV	0.016	0.608	0.026	X	0.017	0.999	0.992	X

Table 5.6: Power of χ^2 statistical tests for 100 fb^{-1} with a=0.01.

Reference	ϕ				$\cos\theta$			
	SM	Odd	Even	CPV	SM	Odd	Even	CPV
SM	X	0.401	0.024	0.00999	X	0.973	0.384	0.033
Odd	0.526	X	0.227	0.395	0.983	X	0.999	0.934
Even	0.028	0.124875	X	0.015	0.917	0.999	X	0.971
CPV	0.014	0.268	0.015	X	0.00899	0.906	0.62	X

Table 5.7: Power of χ^2 statistical tests for 50 fb^{-1} with a=0.01.

where W is the sum of the covariance matrices for each hypothesis, and $\vec{\mu}$ are the means of each hypothesis in the two tests. Once the a_i for each test are calculated, the results from each pseudo-experiment are then reprocessed to measure the distribution of the new test statistic, t_χ. Figure 5.13 shows the distributions of the new test statistic, with the position of a marked with an arrow. As shown in Table 5.9, the power of the test is not markedly improved by combining the two observables.

A strong advantage of this test is that the most important theoretical case, discriminating between Standard Model and CP-odd cases, is fortunately also the easiest hypothesis to test. The downside of this method is that the ABC parameter space is essentially infinite, and it would be unfeasible to generate reference histograms for all possible circumstances. This would be especially problematic if the most likely outcomes – the Standard Model scalar and supersymmetric pseudoscalar cases – are excluded.

Reference	ϕ				$\cos\theta$			
	SM	Odd	Even	CPV	SM	Odd	Even	CPV
SM	X	0.0819	0.0339	0.0269	X	0.251	0.0209	0.0119
Odd	0.0669	X	0.0349	0.0609	0.215	X	0.748	0.206
Even	0.0129	0.0169	X	0.00999	0.336	0.946	X	0.410
CPV	0.00999	0.0249	0.0159	X	0.0329	0.271	0.0789	X

Table 5.8: Power of χ^2 statistical tests for 10 fb^{-1} with a=0.01.

Luminosity	Reference Type	Coupling Type			
		SM	Odd	Even	CPV
100	SM	X	0.99	0.466	0.0059
	Odd	0.998	X	0.996	0.996
	Even	0.26	0.704	X	0.199
	CPV	0	0.99	0.514	X
50	SM	X	0.809	0.033	0
	Odd	0.746	X	0.682	0.602
	Even	0.271	0.610	X	0.258
	CPV	0	0 .999	0.729	X
10	SM	X	0.189	0	0
	Odd	0.0169	X	0.154	0.0039
	Even	0.710	0.874	X	0.724
	CPV	0	0.999	0.899	X

Table 5.9: Power of the t statistical tests with a=0.01.

5.3.4 Curve fitting

Directly comparing data to Monte Carlo is a simple but inelegant way to measure the structure of the angular distributions. The method is also limited by the number of MC event samples that can be produced, and it relies on the accuracy of the simulation process. It is desirable, therefore, to analyse these distributions by fitting them to the predicted functional form for each. As shown in Chapter 2, the distribution of ϕ can be parametrized as

$$F(\phi) = 1 + \alpha\cos\phi + \beta\cos 2\phi + \gamma\sin\phi + \delta\sin 2\phi. \tag{5.5}$$

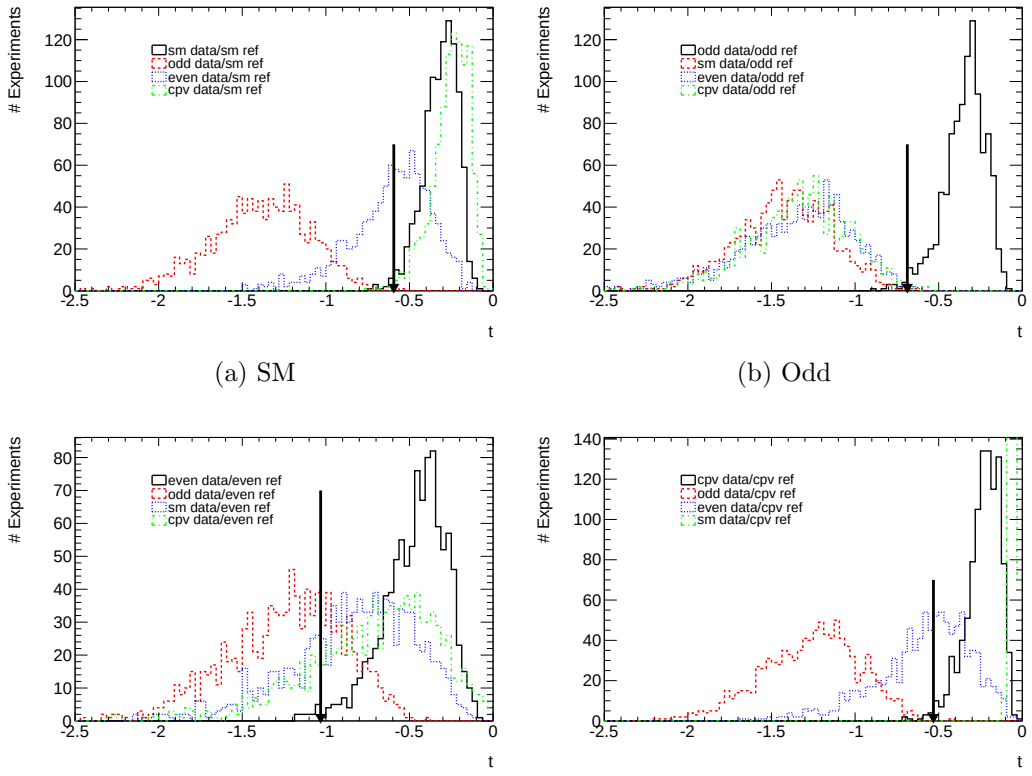

(a) SM (b) Odd

(c) Even (d) CPV

Figure 5.13: Distributions when comparing data-like histograms of the test statistic t_{χ^2} for the four coupling types to each reference histogram, with 100 fb^{-1}. In each Figure, the solid black histogram corresponds to the distribution where the reference is being compared to samples of the same type (null hypothesis), while the other lines correspond to samples of the 3 different types. The arrow corresponds to a significance level of 0.01 for the null hypothesis.

The functional form of the $\cos\theta$ distribution is accessed through the polarization of the Z bosons. This is given by

$$G(\theta) = T(1 + \cos^2\theta) + L\sin^2\theta, \tag{5.6}$$

where T corresponds to the fraction of Z bosons with transverse polarization, and L to the fraction with longitudinal polarization. Since longitudinal and transverse are the only polarization options ($L + T = 1$ is a strict requirement), only their relative

amounts provide useful information. With R as defined in equation 2.15, the equation to fit thus becomes

$$G(\theta) = \left(\frac{R+1}{2}\right)(1+\cos^2\theta) + \left(\frac{1-R}{2}\right)\sin^2\theta \tag{5.7}$$

with R as the useful parameter.

Figure 5.14 shows sample pseudo-experiments for each coupling type for the ϕ distribution, each with the corresponding best fit, and Figure 5.17 shows the same for $\cos\theta$. As before, performing this process for all 1000 experiments provides the probability distribution for each coupling type. These distributions are shown in Figures 5.15, 5.16 and 5.18 for α and β, γ and δ, and R, respectively, and are effectively modelled by Gaussians.

As discussed in the previous section, it is possible to combine the discriminating power of the parameters using a Fisher analysis to calculate a new parameter t_{fit}, which is a linear combination of the original parameters which maximizes the discriminating power of the test. The procedure is performed the same as for the χ^2 case except that there are now 5 coefficients instead of 2.

Each non-Standard Model case is compared to the Standard Model sample, again requiring a significance of 0.01. Table 5.10 shows the power of each possible test. The results are similar to those found above by applying the χ^2 test. By requiring a power of 0.9 to consider a test useful, it is possible to discriminate between the Standard Model null hypothesis and both pure anomalous couplings with 100 fb^{-1}, but not the CPV case. At 50 fb^{-1}, it is not possible to separate the anomalous CP even signal from that of Standard Model results. At the 10 fb^{-1} level, all discriminating power is lost.

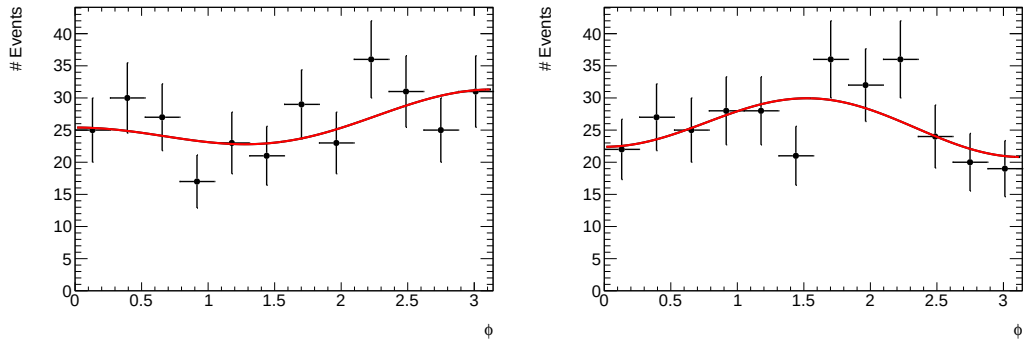

(a) SM: $\alpha_{SM} = -0.114$, $\beta_{SM} = 0.0995$, $\gamma_{SM} = 0.0143$, $\delta_{SM} = 0.02014$

(b) Odd: $\alpha_{ODD} = 0.0309$, $\beta_{ODD} = -0.162$, $\gamma_{ODD} = 0.0191$, $\delta_{ODD} = -0.0117$.

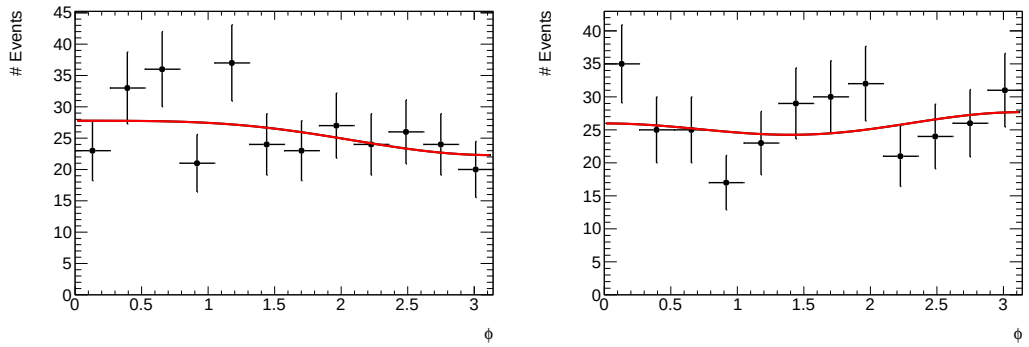

(c) Even: $\alpha_{EVEN} = 0.107$, $\beta_{EVEN} = -0.0253$, $\gamma_{EVEN} = -0.0217$, $\delta_{EVEN} = 0.0047$.

(d) CPV: $\alpha_{CPV} = -0.0335$, $\beta_{CPV} = 0.0489$, $\gamma_{CPV} = -0.0337$, $\delta_{CPV} = -0.0274$.

Figure 5.14: Example pseudo-experiments for each coupling type, at 100 fb^{-1}. The points with error bars represent the distribution in a single simulated experiment. The parameters which result in the best fits in this example are listed below each figure.

5.3.5 Asymmetries

It is apparent from the previous two sections that the Standard Model and CP violating samples are the most difficult to separate using the featured methods. A feature of the distributions that may be used to analyse this situation further is that the CP violating coupling is the only model that shows an inherent asymmetry in some distributions. As discussed in Chapter 2, six asymmetries can be constructed out of the observables ϕ and θ. These observables are labelled as O_i, with $i = \{1...6\}$

Reference	100 fb^{-1}	50 fb^{-1}	10 fb^{-1}
CP-Odd	0.999	0.999	0.375
CP-Even	0.999	0.872	0.056
CPV	0.855	0.314	0.0109

Table 5.10: Power of statistical tests to discriminate between hypotheses using the test statistic t_{fit}, built from the parameters α, β, γ, δ and R using a Fisher analysis.

and are listed, along with their formulas and the coefficients which influence them, in Table 5.11. Also listed are the predicted values for the $A = C = 1, B = 0\, CP$ violating case for the asymmetry in each observable [2]. The asymmetry in the experimental data is measured as

$$A_i = \frac{N(O_i > 0) - N(O_i < 0)}{N(O_i > 0) + N(O_i < 0)} \tag{5.8}$$

where $N(O_i > 0)$ and $N(O_i < 0)$ is the fraction of events greater than or lesser than zero, respectively, for each observable.

Observable	Formula	Coefficients	$\lvert A_i \rvert$
O_1	$\cos\theta_1$	$\Im m(C)$	0.06
O_2	$-\sin\phi \sin\theta_1$	$\Re e(C), \Re e(B^*C)$	0.01
O_3	$\cos\theta_1 \sin\theta_2 \cos\theta_2 \sin\phi$	$\Re e(C), \Re e(B^*C)$	0.07
O_4	$\sin^2\theta_1 \sin^2\theta_2 \sin\phi \cos\phi$	$\Re e(C)$	0.08
O_5	$\sin^2\theta_1 \sin^2\theta_2 \sin\phi [\sin^2\theta_1 \sin^2\theta_2 \cos\phi$-$\cos\theta_1 \cos\theta_2]$	$\Re e(C)$	0.12
O_6	$\sin\theta_1 \cos\theta_1 \sin\theta_2 \sin\phi$	$\Im m(B)$	0.01

Table 5.11: Observables which probe coupling coefficients via asymmetries in their distributions. A_i are the expected measurements [2].

Figure 5.20 shows the distribution of each asymmetry for both the Standard Model and CP violating cases. Upon inspection, these distributions do not show any appreciable difference. Since $\Im m(C) = \Im m(B) = 0$ in all cases, O_1 and O_6 are not expected to show any signal. However, all other observables have $\Re e(C)$ dependancy and thus should show some asymmetry. It is possible to quantify whether or not the asymmetry in a distribution will be a useful test statistic for determining the nature

of the coupling. This will depend on the size of the signal compared to statistical fluctuation in the data. According to Poisson statistics, if the expected value of an asymmetry is zero, there will be statistical fluctuations with a standard deviation of $\sqrt{N}$. The significance (S) of the deviation from zero is therefore $S = A_i \cdot \sqrt{N}$. Figure 5.21 shows the distribution of the significance of each asymmetry for each of 1000 pseudo-experiments. In no case does the significance rise above 3 in more than a small fraction of the cases. The distribution of the significance in all cases follows approximately what would be expected by a normal distribution of the fluctuations, implying that there is no signal to observe. This is consistent with previous work [8] which suggest that, in this mass range, integrated luminosity of greater than 100 fb^{-1} are required to reach a significance level of 3-5σ.

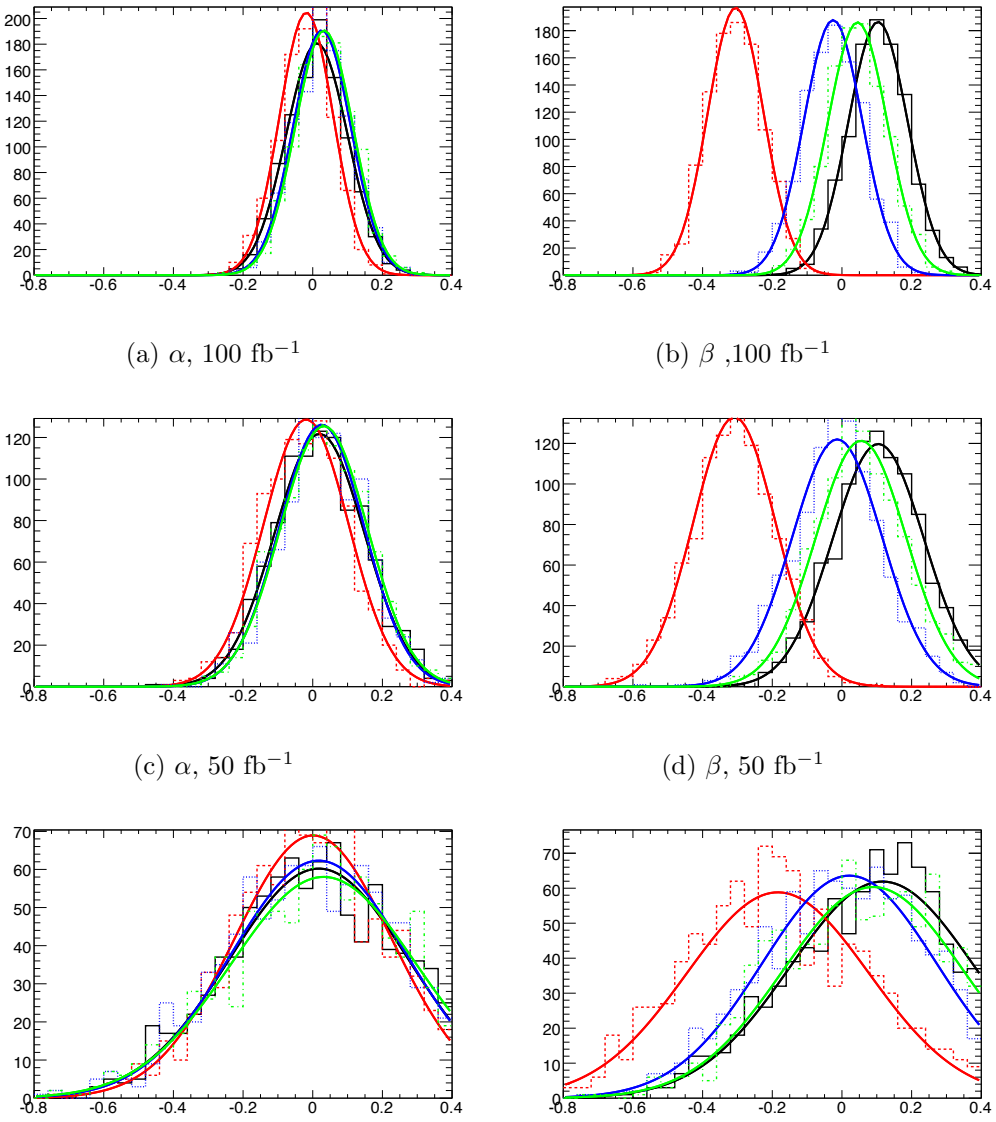

(a) α, 100 fb^{-1}

(b) β ,100 fb^{-1}

(c) α, 50 fb^{-1}

(d) β, 50 fb^{-1}

(e) α, 10 fb^{-1}

(f) β, 10 fb^{-1}

Figure 5.15: Distributions of the α and β parameters in 1000 simulated pseudo-experiments, at luminosities of 10, 50 and 100 fb^{-1}. The histograms are fitted by gaussians, with the Standard Model sample in black, CP-odd in red, CP-even in blue and CPV in green.

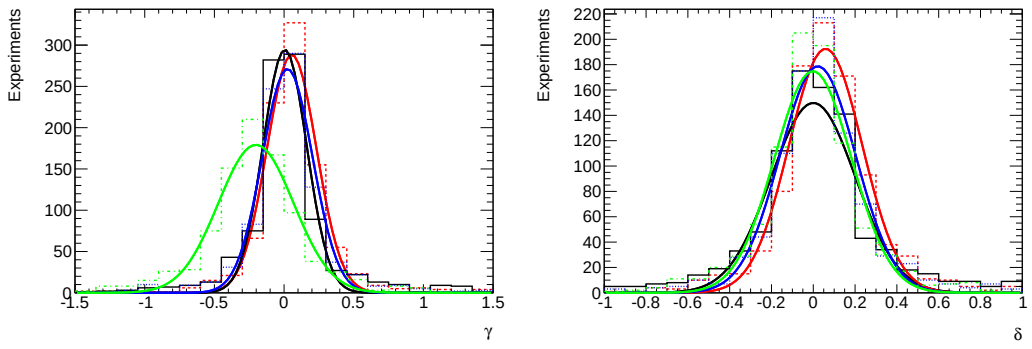

(a) γ, 100 fb^{-1}

(b) δ ,100 fb^{-1}

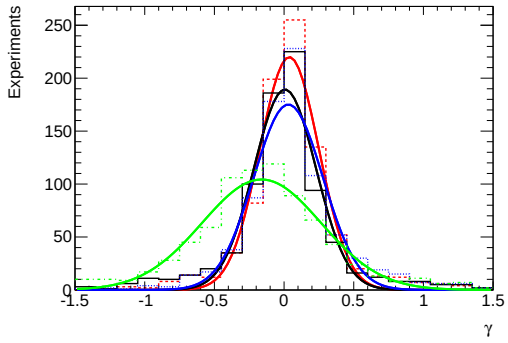

(c) γ, 50 fb^{-1}

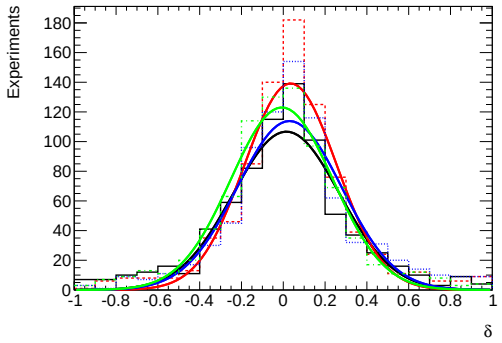

(d) δ ,50 fb^{-1}

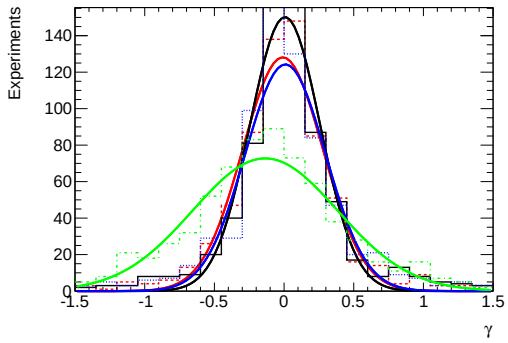

(e) γ, 10 fb^{-1}

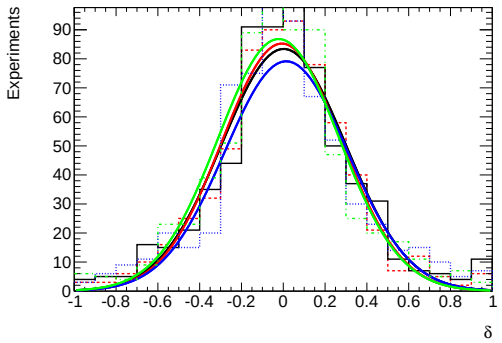

(f) δ ,10 fb^{-1}

Figure 5.16: Distributions of the γ and δ parameters in 1000 simulated pseudo-experiments, at luminosities of 10, 50 and 100 fb^{-1}. The histograms are fitted by gaussians, with the Standard Model sample in black, CP-odd in red, CP-even in blue and CPV in green.

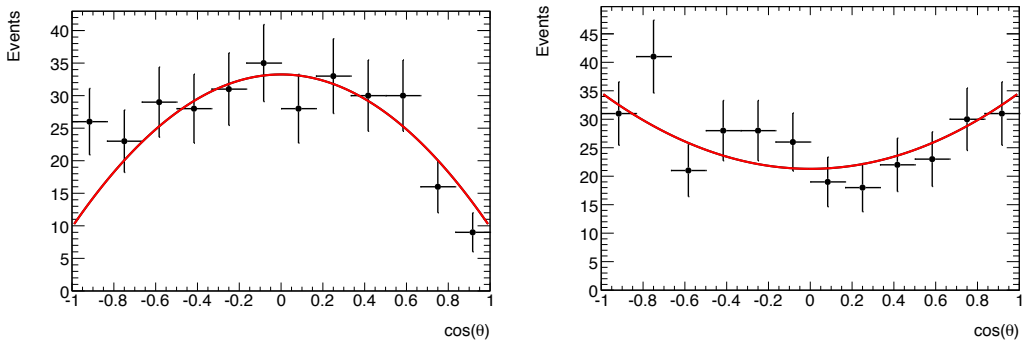

(a) SM

(b) Odd

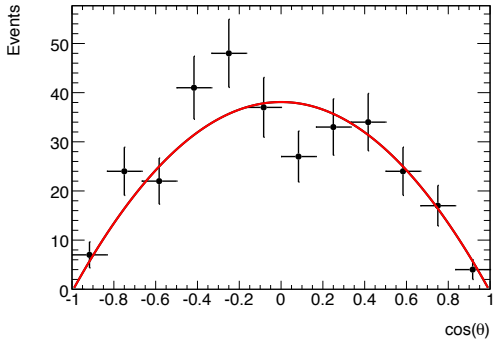

(c) Even

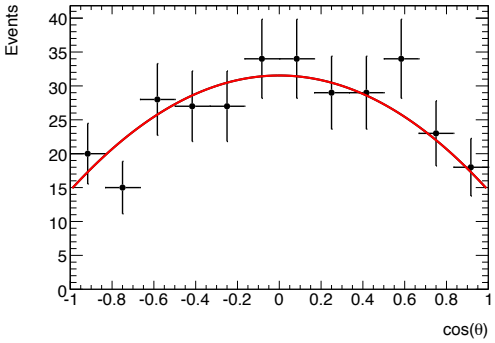

(d) CPV

Figure 5.17: Example pseudo-experiments for each coupling type, at 100 fb^{-1}. In this example, the resulting best fits are $R_{SM} = 0.707$, $R_{ODD} = -0.630$, $R_{EVEN} = 1.014$, $R_{CPV} = 0.539$

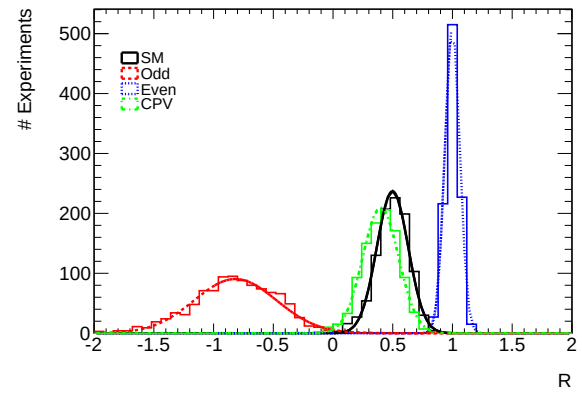

(a) 100 fb^{-1}

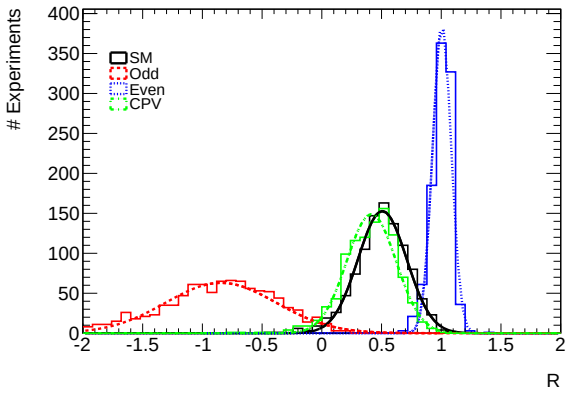

(b) 50 fb^{-1}

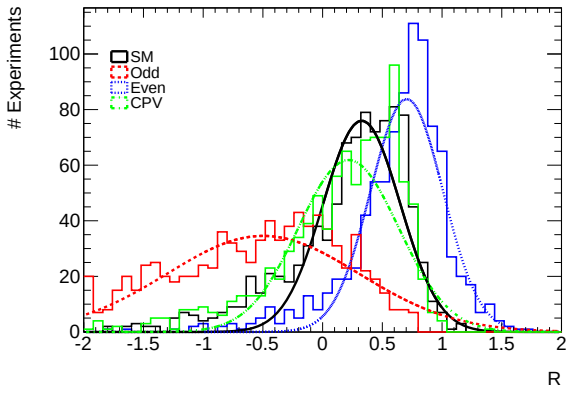

(c) 10 fb^{-1}

Figure 5.18: Distribution of R values, obtained from maximum likelihood fits of 1000 pseudo-experiments of each type at 100 fb^{-1}, 50 fb^{-1},and 10 fb^{-1} of integrated luminosity. Also shown are fit lines modelling the R distributions as gaussian.

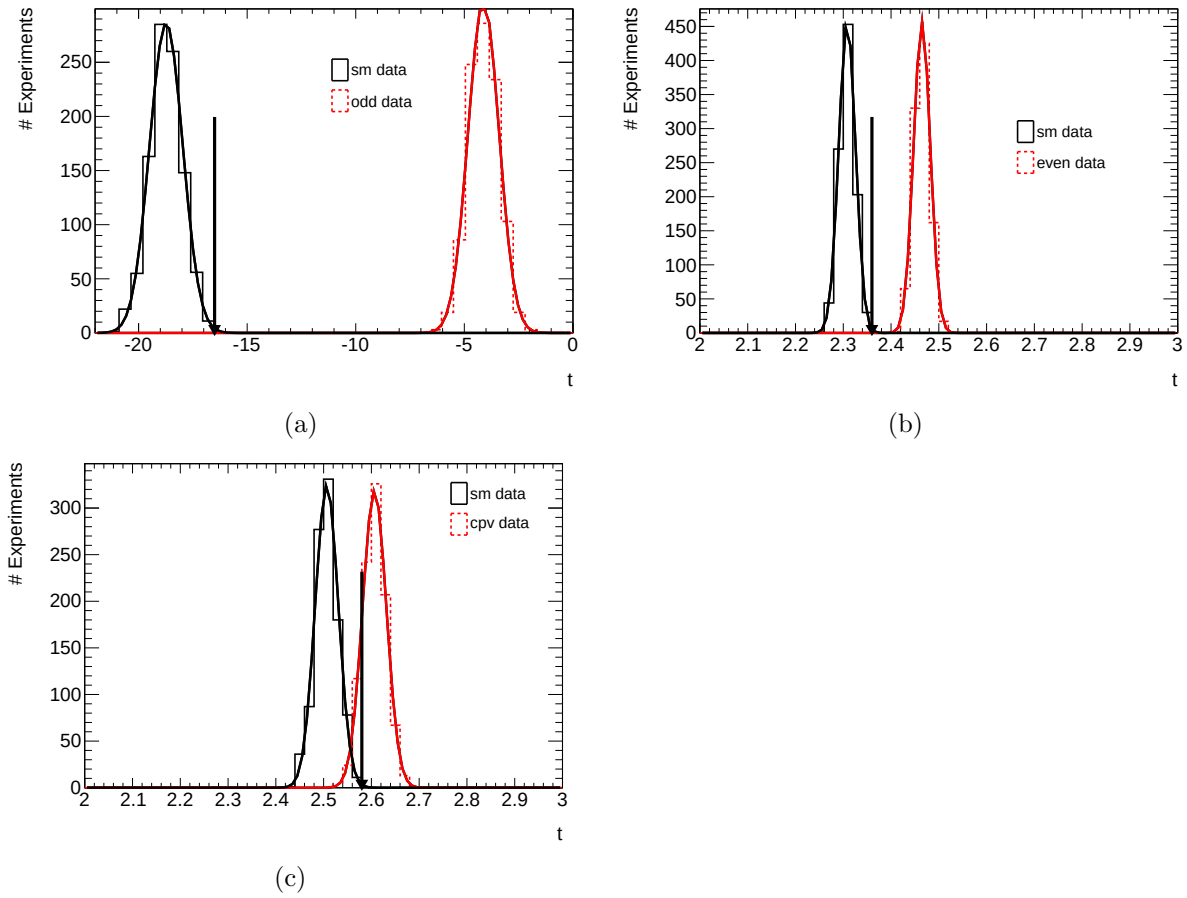

Figure 5.19: Distribution of t_{fit} values, obtained from maximum likelihood fits of 1000 pseudo-experiments of each type at 100 fb^{-1}. Also shown are fit lines modelling the t_{fit} distributions as gaussian. The arrow points to the cutoff a=0.01 for the Standard Model null-hypothesis.

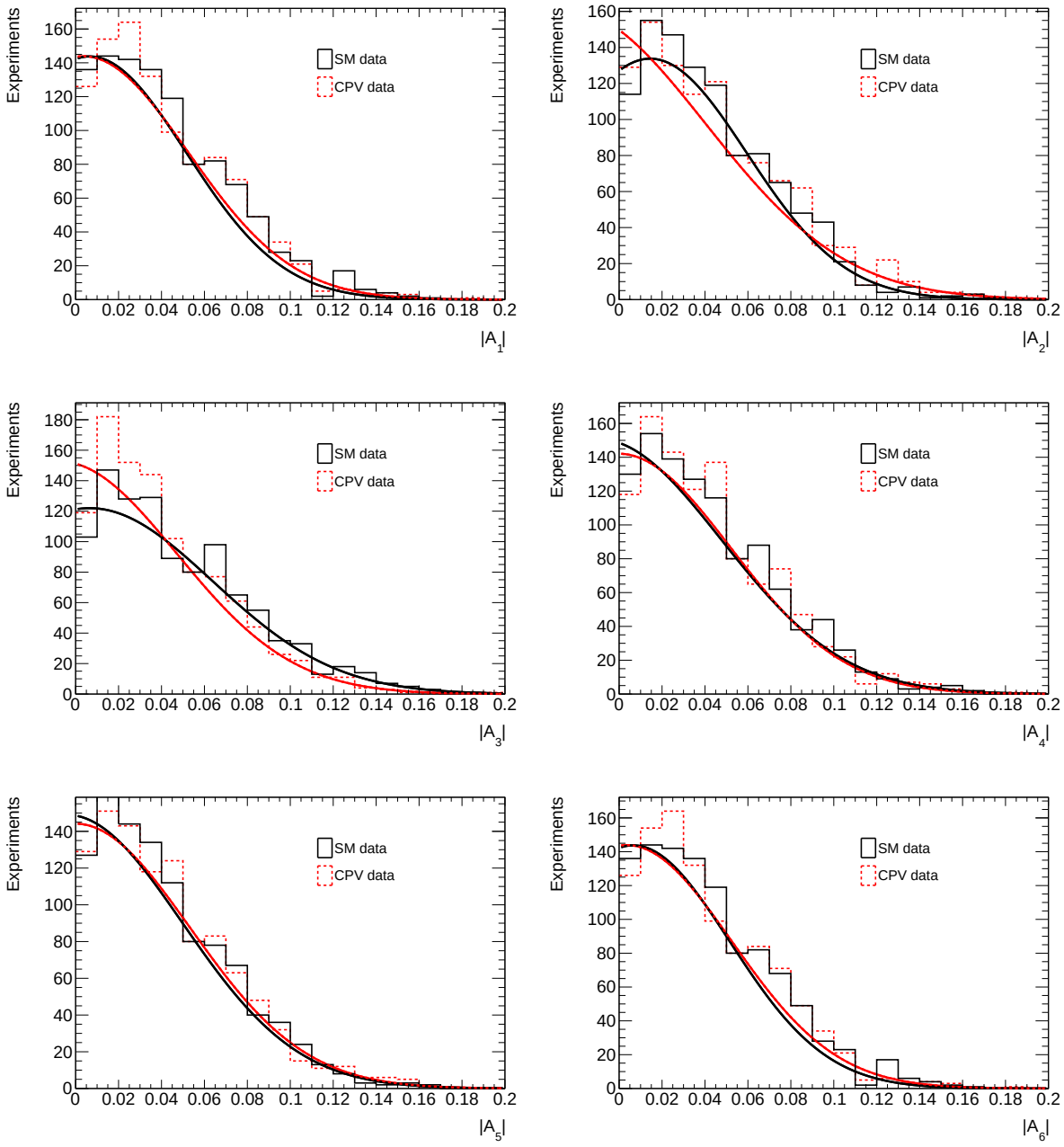

Figure 5.20: Distribution of the 6 asymmetries in 1000 pseudo-experiments, for CP-violating and Standard Model coupling types.

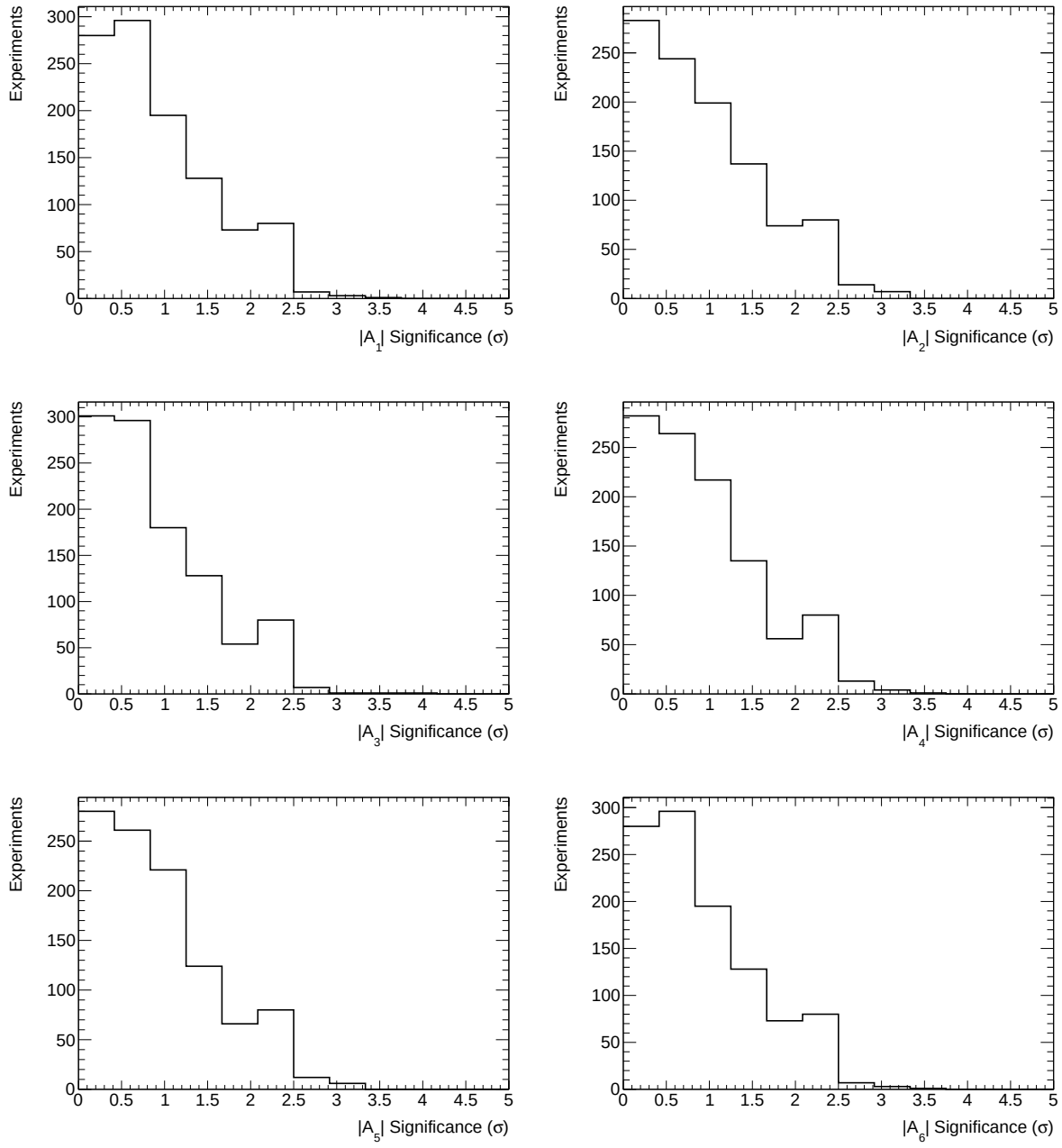

Figure 5.21: Distribution of the statistical significance, in σ, of the 6 asymmetries in 1000 pseudo-experiments for the CP-violating coupling type.

Chapter 6

Conclusion

In several years time, when the LHC is expected to have provided the ATLAS detector with enough pp collisions to observe the Higgs boson, ATLAS should be well equipped to make definitive statements about the nature of the new particle. The primary interest will be towards identifying whether the Higgs signal is consistent with a scalar particle, as predicted by the Standard Model, or a pseudoscalar particle which is a possibility in the Minimal Supersymmetric Model. This work has shown that it should be possible to make this distinction clearly with 50 fb^{-1} at 0.01 significance, either by direct comparison to Monte Carlo or by measuring fit parameters. Upwards of 100 fb^{-1} will be required to distinguish between the Standard Model scalar and a non-Standard Model scalar coupling. The CP violating case studied here was found to be indistinguishable from the Standard Model case at the integrated luminosities examined.

There are several opportunities for further work in this area. For simplicity, this work ignored the fact that the Standard Model cross-section for Higgs production is expected to differ from that of the MSSM. Precision cross section measurements could be an additional statistic to add to this analysis. Work also needs to be done to

expand the CP violation analysis shown here. Modelling additional combinations of A, B and C at varying luminosities will provide more information about what levels of CPV it will be possible to discover in the Higgs sector at ATLAS.

Bibliography

[1] The ATLAS Collaboration, *Expected performance of the ATLAS experiment: detector, trigger and physics*. Geneva: CERN, 2009.

[2] R. M. Godbole, D. J. Miller, and M. M. Muhlleitner, "Aspects of CP violation in the HZZ coupling at the LHC," *JHEP*, vol. 12, p. 031, 2007.

[3] C. Anastopoulos and et al, "ATLAS sensitivity prospects for the Standard Model Higgs boson in the decay channel $h \to ZZ^{(*)} \to 4\ell$ at $\sqrt{s} = 10$ and 7 tev," Tech. Rep. ATL-COM-PHYS-2010-227, CERN, Geneva, May 2010.

[4] J. Goldstone, A. Salam, and S. Weinberg, "Broken symmetries," *Phys. Rev.*, vol. 127, pp. 965–970, Aug 1962.

[5] P. W. Higgs, "Spontaneous symmetry breakdown without massless bosons," *Physical Review*, vol. 145, no. 4, pp. 1156–1163, 1966.

[6] D. Griffiths, *Introduction to Elementary Particles*. John Wiley and Sons, Inc., 1987.

[7] B. W. Lee, C. Quigg, and H. B. Thacker, "Weak interactions at very high energies: The role of the Higgs-boson mass," *Phys. Rev. D*, vol. 16, pp. 1519–1531, Sep 1977.

[8] J. H. Christenson, J. W. Cronin, V. L. Fitch, and R. Turlay, "Evidence for the 2π decay of the K_2^0 meson," *Phys. Rev. Lett.*, vol. 13, pp. 138–140, Jul 1964.

[9] B. Aubert and et al., "Observation of CP violation in the B^0 meson system," *Phys. Rev. Lett.*, vol. 87, p. 091801, Aug 2001.

[10] S. Y. Choi, D. J. Miller, M. M. Muehlleitner, and P. M. Zerwas, "Identifying the Higgs spin and parity in decays to Z pairs," *Physics Letters B*, vol. 553, no. 1-2, pp. 61 – 71, 2003.

[11] A. Straessner, "Prospects for the measurement of CP parameters of the higgs boson in $H \to ZZ \to 4\ell$ decays with the ATLAS detector," Tech. Rep. ATL-COM-PHYS-2008-065, CERN, Geneva, May 2008.

[12] The ATLAS Collaboration, "The ATLAS experiment at the CERN Large Hadron Collider," *Journal of Instrumentation*, vol. 3, no. 08, p. S08003, 2008.

[13] D. H. Perkins, *Introduction to High Energy Physics*. Cambridge: Cambridge University Press, 2000.

[14] K. Kordas and et al., "The ATLAS data acquisition and trigger: concept, design and status," Tech. Rep. ATL-DAQ-CONF-2007-022. ATL-COM-DAQ-2007-015, CERN, Geneva, Nov 2006.

[15] T. Sjostrand, S. Mrenna, and P. Skands, "Pythia 6.4 physics and manual," FERMILAB-PUB-06-052-CD-T.

[16] P. Golonka and Z. Was, "Next to Leading Logarithms and the PHOTOS Monte Carlo," *Eur. Phys. J.*, vol. C50, pp. 53–62, 2007.

[17] J. Pumplin and et al., "New generation of parton distributions with uncertainties from global QCD analysis," *JHEP*, vol. 07, p. 012, 2002.

[18] N. Andari and et al., "Higgs production cross sections and decay branching ratios," Tech. Rep. ATL-COM-PHYS-2010-046, CERN, Geneva, Jan 2010.

[19] S. Agostinelli and et al., "G4–a simulation toolkit," *Nuclear Instruments and Methods in Physics Research Section A: Accelerators, Spectrometers, Detectors and Associated Equipment*, vol. 506, no. 3, pp. 250 – 303, 2003.

[20] A. Straessner. Private Communication, 2010.

[21] S. Hassani, L. Chevalier, E. Lanon, J.-F. Laporte, R. Nicolaidou, and A. Ouraou, "A muon identification and combined reconstruction procedure for the ATLAS detector at the LHC using the (MUONBOY, STACO, MuTag) reconstruction packages," *Nuclear Instruments and Methods in Physics Research A*, vol. 572, no. 1, pp. 77 – 79, 2007. Frontier Detectors for Frontier Physics - Proceedings of the 10th Pisa Meeting on Advanced Detectors.